

This is the accepted manuscript made available via CHORUS. The article has been published as:

Crystal structures, frustrated magnetism, and chemical
pressure in Sr-doped $\text{Ba}_{1-x}\text{Ni}_x\text{Sb}_2\text{O}_9$ perovskites

Mélanie Viaud, Catherine Guillot-Deudon, Eric Gautron, Maria Teresa Caldes, Guido Berlanda, Philippe Deniard, Philippe Boullay, Florence Porcher, Carole La, Céline Darie, A. Zorko, A. Ozarowski, Fabrice Bert, Philippe Mendels, and Christophe Payen

Phys. Rev. Materials **6**, 124408 — Published 20 December 2022

DOI: [10.1103/PhysRevMaterials.6.124408](https://doi.org/10.1103/PhysRevMaterials.6.124408)

Crystal structures, frustrated magnetism and chemical pressure in Sr-doped Ba₃NiSb₂O₉ perovskites

Mélanie Viaud¹, Catherine Guillot-Deudon¹, Eric Gautron¹, Maria Teresa Caldes¹, Guido Berlanda², Philippe Deniard¹, Philippe Boullay³, Florence Porcher⁴, Carole La⁵, Céline Darie⁶, A. Zorko^{7,8}, A. Ozarowski⁹, Fabrice Bert², Philippe Mendels^{2,*} and Christophe Payen^{1,*}

¹ *Nantes Université, CNRS, Institut des Matériaux de Nantes Jean Rouxel, IMN, F-44000
Nantes, France*

² *Laboratoire de Physique des Solides, Université Paris-Saclay, CNRS, 91405 Orsay, France*

³ *CRISMAT laboratory, UMR6508, Normandie University, ENSICAEN, UNICAEN, CNRS,
Caen, 14050 France*

⁴ *Laboratoire Léon Brillouin, CEA Saclay, CNRS UMR12, F-91191 Gif-sur-Yvette, France*

⁵ *Nantes Université, CNRS, UMR 6112, Laboratoire de Planétologie et Géosciences, F-44000
Nantes, France*

⁶ *Univ. Grenoble Alpes, CNRS, Grenoble INP, Institut Néel, 38000 Grenoble, France*

⁷ *Jožef Stefan Institute, Jamova c. 39, 1000 Ljubljana, Slovenia*

⁸ *Faculty of Mathematics and Physics, University of Ljubljana, Jadranska u. 19, 1000
Ljubljana, Slovenia*

⁹ *National High Magnetic Field Laboratory, Florida State University, Tallahassee, Florida
32310, USA*

*corresponding author: philippe.mendels@universite-paris-saclay.fr

*corresponding author: christophe.payen@cnrs-imn.fr

Revised version for APS Journal Service Dept. - November 2022

ABSTRACT

The effects of chemical pressure on the structural and magnetic properties of the triple perovskite $\text{Ba}_3\text{NiSb}_2\text{O}_9$ are investigated by substituting Sr^{2+} ions for Ba^{2+} ions. Two $\text{Ba}_{3-x}\text{Sr}_x\text{NiSb}_2\text{O}_9$ phases could be stabilized via a solid-state reaction at ambient pressure (AP) in air. The 6H with Sb_2O_9 pairs ($x = 0$) \rightarrow 6H with NiSbO_9 pairs ($x = 0.5$) \rightarrow 3C (cubic with corner-sharing octahedral, $x = 1.25$) sequence of structural phases occurs with increasing Sr content, i.e. chemical pressure, which is similar to that previously reported for pure samples of $\text{Ba}_3\text{NiSb}_2\text{O}_9$ obtained under increasing high physical pressure (HP). For the 6H $\text{Ba}_{2.5}\text{Sr}_{0.5}\text{NiSb}_2\text{O}_9$ ($x = 0.5$) phase, using combined Rietveld refinements of powder X-ray and neutron diffraction patterns, precession electron diffraction tomography (PEDT) data collected on thin crystals, aberration corrected high-angle annular dark field scanning transmission electron microscopy (HAADF-STEM) coupled to energy dispersive X-ray spectroscopy (EDX) mapping, we reach the conclusion that the structure features corner-sharing SbO_6 octahedra and NiSbO_9 pairs of face-shared octahedra (or Ni-Sb “dumbbells”) with either a random orientation of the Ni-Sb dumbbells or nanosized chemical correlations for the dumbbell arrangement. As observed in HP $\text{Ba}_3\text{NiSb}_2\text{O}_9$ produced through synthesis at 9 GPa, AP $\text{Ba}_{1.75}\text{Sr}_{1.25}\text{NiSb}_2\text{O}_9$ ($x = 1.25$) crystallizes in a 3C double perovskite $\text{A}_2\text{BB}'\text{O}_6$ cubic structure where A, B and B' sites are occupied by (Ba+Sr), Sb and ($2/3\text{Ni} + 1/3\text{Sb}$) atoms, respectively. The B' sites, which are randomly occupied by spin-1 Ni^{2+} and diamagnetic Sb^{5+} , form a face-centered-cubic (FCC) sublattice where the Ni^{2+} amount stays above the site percolation threshold. Weiss temperatures (≈ -65 K and ≈ -213 K for $\text{Ba}_{2.5}\text{Sr}_{0.5}\text{NiSb}_2\text{O}_9$ and $\text{Ba}_{1.75}\text{Sr}_{1.25}\text{NiSb}_2\text{O}_9$, respectively) indicate that dominant magnetic interactions between Ni^{2+} spins are antiferromagnetic with magnitudes similar to those observed in the corresponding HP phases of pure $\text{Ba}_3\text{NiSb}_2\text{O}_9$. As for the 6H HP $\text{Ba}_3\text{NiSb}_2\text{O}_9$ compound, in 6H $\text{Ba}_{2.5}\text{Sr}_{0.5}\text{NiSb}_2\text{O}_9$, muon spin relaxation (μSR) measurements identify a dynamic magnetic state down to the base temperature (95 mK), consistent with a previously published inelastic neutron scattering (INS) study. For 3C $\text{Ba}_{1.75}\text{Sr}_{1.25}\text{NiSb}_2\text{O}_9$, μSR and ^{121}Sb NMR measurements both indicate the presence of a transition to a static magnetic state below 11(1) K with a significant amount of disorder in this frozen state, in contrast to the spin-liquid state previously suggested for the 3C HP phase of $\text{Ba}_3\text{NiSb}_2\text{O}_9$. Consistently, a broad maximum is observed in the specific heat at the same temperature. Building on the structural data, the magnetic properties of HP 6H $\text{Ba}_3\text{NiSb}_2\text{O}_9$ and AP 6H $\text{Ba}_{2.5}\text{Sr}_{0.5}\text{NiSb}_2\text{O}_9$ are discussed in the light of recent works on triangular and J_1 - J_2

honeycomb systems with or without quenched disorder. We are led to the conclusion that the driving force towards a spin-liquid like state is quenched disorder which needs to be incorporated in J_1 - J_2 honeycomb models. Our evidence of a magnetic transition to a frozen magnetic ground state for the AP Sr-doped 3C phase is in line with models for geometrically frustrated FCC antiferromagnets. This calls for a better experimental and possibly theoretical understanding of the HP 3C phase.

I. INTRODUCTION

Over the last decades, the study of frustrated spin models and frustrated magnetic materials has opened new avenues in the field of magnetism. It has indeed produced a wealth of novel magnetic phases whose stabilization depends on the nature of frustration originating from the crystal structure. This spans a wide variety from exotic quantum spin liquids (QSL) or valence bond solid (VBS) phases to finely frustration-tuned long range ordered states where quantum fluctuations survive. They can be stabilized on a variety of 2D or 3D spin lattices, e.g., triangular, kagome, J_1 - J_2 honeycomb, pyrochlore, face-centered-cubic (FCC) which can be realized in some transition metal or rare earth solid-state compounds. Yet, identifying the spin Hamiltonian parameters and the associated various energy scales for real systems proves in many cases to be difficult even when average crystal structures are known accurately. In a context where frustration generates many possible and close-by in energy competing states, this constitutes a bottleneck in the comparison to ideal models still under study.

Within the past few years, the realm of materials has also led to consideration of the impact of disorder on ground state selection. For instance, the recently discovered triangular-lattice-based material YbMgGaO_4 [1–3], which harbors an unexpected spin liquid-like ground state, has been the subject of significant discussions. The main issues are the determination of its exchange parameters and the role of intrinsic structural disorder associated with the random occupation of the same crystallographic position by non-magnetic Mg^{2+} and Ga^{3+} ions [4,5]. This in turn triggered new conceptual approaches encompassing disorder [6] which might shed new light on the physics of numerous frustrated materials.

The family of triple-perovskite materials $\text{Ba}_3\text{MSb}_2\text{O}_9$ ($M = \text{Co}, \text{Ni}, \text{Cu}$) has recently received a good deal of attention since some of these insulating oxides were identified as realizations of triangular lattice antiferromagnets or as candidates for quantum spin-liquid (QSL) states [7–12]. These materials exhibit an even richer variety of structural and magnetic properties. The 6H perovskite $\text{Ba}_3\text{CoSb}_2\text{O}_9$, for instance, comprises a long-sought triangular lattice of $S_{\text{eff}}=1/2$ Co^{2+} which exhibits a field-induced up-up-down phase and quantum fluctuations effects in its magnon spectrum [13–15]. The $S=1/2$ Cu^{2+} compound shows considerable deviation from this archetypal triangular antiferromagnetic lattice because of differences in crystal structures. Indeed, in the 6H structure of $\text{Ba}_3\text{CuSb}_2\text{O}_9$, B sites of the B_2O_9 face-sharing bi-octahedra are occupied by Sb^{5+} and Cu^{2+} ions leading to the formation of asymmetric Cu-Sb “dumbbells”

exclusively (instead of Sb-Sb dumbbells as for 6H $\text{Ba}_3\text{CoSb}_2\text{O}_9$) [10]. An experimental and theoretical consensus has emerged from numerous studies showing that, at the local structural level, these dumbbells arrange in a very short-range honeycomb lattice with strong disorder [10,16–19]. The resulting state does not show any magnetic ordering, but does display strong orbital correlations, and its ground state is referred to as a quantum spin-orbital entangled liquid [20].

As for the Ni^{2+} ($S=1$) nickel-based perovskites, which are the focus of this paper, a QSL state was suggested in the so-called “6HB” high-pressure (HP) phase of $\text{Ba}_3\text{NiSb}_2\text{O}_9$ [12]. This 6HB compound is prepared in polycrystalline form by treating the so-called “6HA” ambient pressure (AP) polytype of $\text{Ba}_3\text{NiSb}_2\text{O}_9$ under a pressure of a few GPa [12,21]. The HP 6HB form differs from the AP 6HA phase in that its crystal structure consists of NiSbO_9 pair of face-sharing octahedral, or Ni-Sb dumbbell (instead of Sb_2O_9 bi-octahedra as for the 6HA form), connected by their vertices to single corner-sharing SbO_6 octahedra (instead of NiO_6 octahedra as for the 6HA phase) [12,21,22]. In the $P6_3mc$ hexagonal crystal structure of 6HB $\text{Ba}_3\text{NiSb}_2\text{O}_9$ as described by Cheng et al. on the basis of X-ray diffraction data [12], the Ni-Sb dumbbells all have the same vertical orientation (‘all-up’ arrangement) so that the Ni^{2+} ions form a spin-1 - less studied than $S=1/2$ - triangular lattice within each triangular layer of NiSbO_9 bi-octahedra (Fig. 1(a)). The magnetic triangular lattices are stacked along the hexagonal c -axis and are separated from each other by two nonmagnetic layers of SbO_6 octahedra. A more recent structural investigation of independently prepared samples of HP 6HB $\text{Ba}_3\text{NiSb}_2\text{O}_9$ revealed a different crystal structure [23]. Combined Rietveld refinements of powder X-ray and neutron diffraction patterns were obtained with the distinct hexagonal centrosymmetric S.G. $P6_3/mmc$. Furthermore, precession electron diffraction on thin crystals indicated that the actual symmetry is at most trigonal. Nonetheless, the HP phase was still termed 6HB in subsequent works on its magnetic properties. To reconcile differences between powder diffraction and electron diffraction results, it was suggested that crystallites contain domains of small dimensions (1-10 nm) in which the orientations of the Ni-Sb dumbbells alternate between adjacent $(\text{NiSbO}_9)_\infty$ bilayers; in each domain, an ‘up-down’ or ‘down-up’ stacking is observed along the c -axis, as shown in Fig. 1(b). The Ni triangular layers are therefore separated from each other alternately by one and three layers of nonmagnetic SbO_6 octahedra (instead of two for the $P6_3mc$ structure in ref. [12]). Because two adjacent Ni ions that are separated by only one nonmagnetic SbO_6 layer along the c axis are likely to interact via Ni-O-O-Ni superexchange, Quilliam et al. [24] suggested that the structure contains magnetic bilayers described by a J_1 - J_2 buckled honeycomb

model at the local level (Fig. 1(b)). The bulk magnetic susceptibility was very similar to that reported earlier [12], showing a Weiss temperature of - 76 K [24]. Muon spin rotation (μ SR) and ^{121}Sb NMR measurements showed that it exhibits a gapless QSL-like ground state [24]. No static magnetism was indeed observed down to temperature as low as 20 mK. NMR results further suggested some structural disorder of unknown origin. Upon applying pressure up to 9 GPa, 6H $\text{Ba}_3\text{NiSb}_2\text{O}_9$ transforms into a cubic 3C phase with total elimination of face-sharing octahedra [12], as observed in HP $\text{Ba}_3\text{ZnSb}_2\text{O}_9$ [21]. This 3C phase can be described as a $\text{Ba}_2\text{BB}'\text{O}_6$ double cubic perovskite where BO_6 and $\text{B}'\text{O}_6$ corner-sharing octahedra are occupied by Sb and $(2/3\text{Ni} + 1/3\text{Sb})$ atoms, respectively (Fig. 2) [12]. The B' sites form a face-centered-cubic (FCC) sublattice. This 3C HP phase of $\text{Ba}_3\text{NiSb}_2\text{O}_9$ was also identified as candidate spin-liquid compounds with a Weiss temperature of -180 K [12].

In this work, we explore a different route to obtain 6H and 3C phases by replacing Ba^{2+} with Sr^{2+} in $\text{Ba}_3\text{NiSb}_2\text{O}_9$. The Sr^{2+} ion, which is smaller in size than Ba^{2+} (ionic radii 1.44 versus 1.61 Å in 12-coordinate [25]), can be used as a chemical substituent for generating chemical pressure and thus for tuning the structural and magnetic properties of Ba-containing perovskites [26–28]. Here, our goal is to prepare and characterize thermodynamically stable phases that may host quantum paramagnetic states including QSL. Polycrystalline samples of $\text{Ba}_{3-x}\text{Sr}_x\text{NiSb}_2\text{O}_9$ with nominal $x \leq 1.25$ have been prepared at ambient pressure conditions. The structural and magnetic properties of two particular single-phased Sr-substituted samples, namely 6H $\text{Ba}_{2.5}\text{Sr}_{0.5}\text{NiSb}_2\text{O}_9$ ($x = 0.5$) and 3C $\text{Ba}_{1.75}\text{Sr}_{1.25}\text{NiSb}_2\text{O}_9$ ($x = 1.25$) have been studied using diffraction techniques, electron microscopy, bulk susceptibility, ^{121}Sb NMR, and μ SR experiments in order to identify unambiguously their magnetic ground states. Results obtained for these two AP Sr-substituted compounds have been compared to published works related to the corresponding HP phases of pure $\text{Ba}_3\text{NiSb}_2\text{O}_9$. A previously published inelastic neutron scattering (INS) study of a polycrystalline sample of 6H $\text{Ba}_{2.5}\text{Sr}_{0.5}\text{NiSb}_2\text{O}_9$ obtained via the same AP synthesis method evidenced the absence of long-range magnetic order down to 0.05 K and suggested that the magnetic excitation spectrum is characteristic of a spin liquid [29]. Our paper ends with a discussion of these results in the framework of existing models with respect to the possible schemes of magnetic interactions, which for both the 6H and 3C phases, should certainly encompass a strong disorder component.

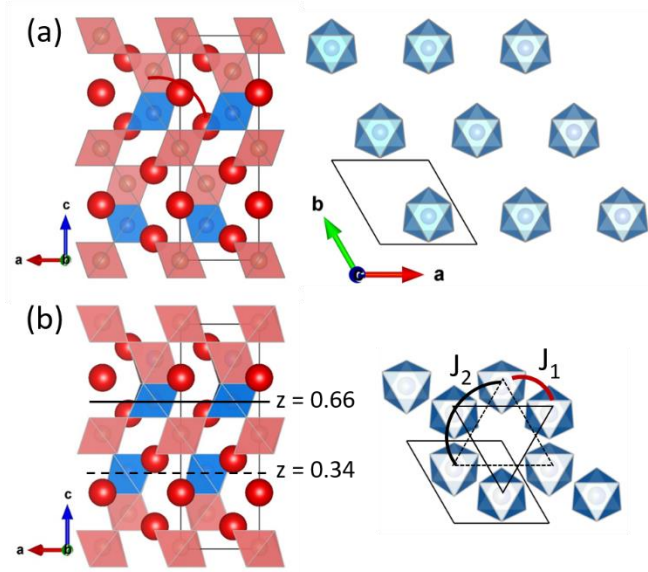


Figure 1. Reported room temperature crystal structures the so-called 6HB high-pressure form of Ba₃NiSb₂O₉. These structures contain NiSbO₉ pairs of face-sharing octahedra (Ni-Sb dumbbells), connected by their vertices to single SbO₆ octahedra. SbO₆ and NiO₆ octahedra are shaded pink and blue, respectively. Red spheres represent Ba²⁺ ions. Thin solid lines depict unit cells. **(a)** P6₃mc hexagonal structure (*a*=5.7925(2) Å; *c*=14.2918(6) Å) with ‘all-up’ arrangement of Ni-Sb dumbbells [12], viewed along the *b* axis. Ni²⁺ ions form AB-stacked triangular lattices in the *ab* plane (right). **(b)** One of the two possible domains with trigonal symmetry, S.G. P3, and ‘down-up’ stacking of Ni-Sb dumbbells along the *c* axis [23]. The other type of domain (not shown) has a reversed ‘up-down’ stacking of Ni-Sb dumbbells, so that the average structure over many domains is described in the centrosymmetric S.G. P6₃/mmc (*a*=5.7926(2) Å; *c*=14.2841(6) Å). In each domain, two adjacent Ni layers (visualized with horizontal lines at *z* = 0.34 and 0.66), which are separated from each other by only one layer of nonmagnetic Sb, forms a *J*₁-*J*₂ honeycomb bilayer (right) [24]. *J*₁ and *J*₂ are the inter-plane and in-plane couplings, respectively.

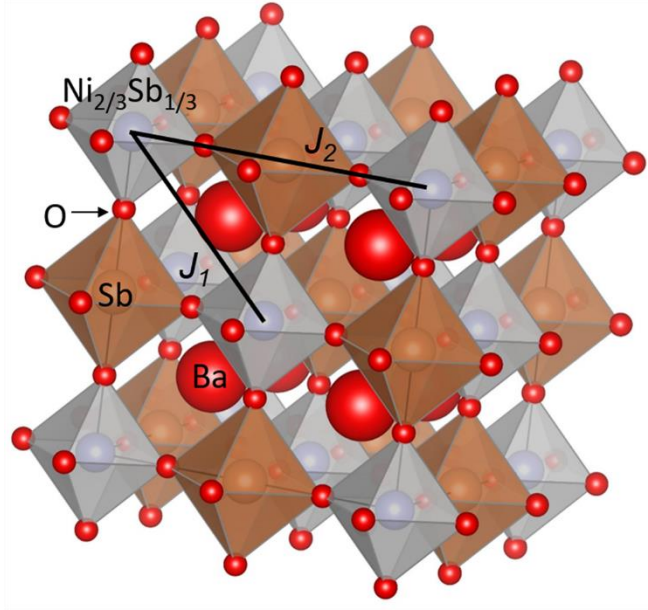


Figure 2. Room-temperature $Fm\bar{3}m$ structure adopted by 3C phase of $Ba_3NiSb_2O_9$ produced at 9 GPa [12]. This phase has a $Ba_2BB'O_6$ double cubic perovskite structure with the BO_6 octahedra occupied by Sb and the B' octahedral sites in a random manner by $(2/3Ni + 1/3Sb)$ atoms. The B' octahedral sites form an undistorted face-centered-cubic (FCC) sublattice. J_1 and J_2 are the nearest-neighbor and next-nearest neighbor interaction between Ni^{2+} ions.

II. EXPERIMENTAL METHODS

Two independent series of powder samples of $Ba_{3-x}Sr_xNiSb_2O_9$ with targeted compositions $x = 0, 0.1, 0.25, 0.5, 0.75, 1,$ and 1.25 were prepared by using a conventional solid-state reaction route at AP [30]. Samples were furnace cooled at the end of the final heat treatment to avoid quenching high-temperature disordered structural arrangements. The samples were characterized using several techniques, including laboratory powder X-ray diffraction (XRD), Scanning Electron Microscopy (SEM) and Energy Dispersive X-ray spectroscopy (EDS), Inductive Coupled Plasma (ICP) analysis, and volumetric mass density measurements [30]. For both series, single-phased samples were obtained for $x = 0, 0.1, 0.5,$ and 1.25 , whereas mixtures of two different crystallized phases were observed for other nominal compositions. Initial analyses of XRD patterns suggested that the two single-phased $x = 0$ and 0.1 samples crystallize with the $P6_3/mmc$ crystal symmetry expected for the AP 6HA phase of $Ba_3NiSb_2O_9$ [22]. These initial analyses also suggested that the $x = 0.5$ and 1.25 samples

crystallize with the crystal symmetries initially reported for the 6HB (S.G. $P6_3mc$) and 3C (S.G. $Fm\bar{3}m$) HP phases of $Ba_3NiSb_2O_9$, respectively [12]. Judging from XRD, the 6HA \rightarrow 6HB \rightarrow 3C sequence of structural phases can therefore be stabilized in the case of chemical pressure, similarly as for physical pressure. The refined lattice parameters of the $x = 0.5$ and $x = 1.25$ samples were found to be slightly smaller than those observed for the 6HB and 3C phases of HP $Ba_3NiSb_2O_9$ produced during syntheses at 3 and 9 GPa, respectively [30]. This finding suggests that the substitution-induced chemical pressures are a bit higher than the relaxed external pressure in the corresponding HP samples.

Neutron powder diffraction (NPD) data were collected at 300 K on $Ba_{2.5}Sr_{0.5}NiSb_2O_9$ ($x = 0.5$) and of $Ba_{1.75}Sr_{1.25}NiSb_2O_9$ ($x = 1.25$) powder samples using the 3T2 instrument (incoming wavelength of $\lambda \approx 1.2247$ Å) at Laboratoire Léon Brillouin (CEA Saclay-CNRS). Rietveld analyses of the XRD and NPD data were performed using JANA 2006 [31]. Crystal structures were drawn using VESTA software [32]. As the scattering lengths of Ba, Sr, Ni, Sb and O depend on the diffraction technique employed (X-ray or neutron), combined Rietveld refinements of XRD and NPD patterns were performed to provide more meaningful descriptions of the average structures of the samples. Neutrons scattering lengths b are 5.07, 7.02, 10.3, 5.57, and 5.803 fm for Ba($Z=56$), Sr($Z=38$), Ni($Z=28$), Sb($Z=51$) and O($Z=8$) atoms, respectively. The Ni-Sb contrasts obtained with X-rays and neutrons are opposite; $Z(Ni)/Z(Sb) = 0.549$ and $b_{Ni}/b_{Sb} = 1.849$. As the neutron wavelength is known with less accuracy than that of X-ray, its value was also refined during the procedure. Cell metrics were therefore determined from XRD patterns [30]. The large samples used for the NPD contained a trace amount of $Ba_3SrSb_2O_9$ impurity phase.

Precession electron diffraction tomography (PEDT), was performed with a Jeol 2010 electron microscope (operating at 200 kV with a LaB6 cathode) equipped with a Nanomegas DigiStar precession module and an upper-mounted Gatan ORIUS 200D CCD camera. PEDT data sets of non-oriented patterns were recorded on several different thin crystals of $Ba_{2.5}Sr_{0.5}NiSb_2O_9$. For data collections the precession angle was set to 1.4° with a goniometer tilt step 1° . PEDT data sets were analyzed using the computer programs PETS [33] and JANA 2006 [31].

High-angle annular dark field scanning transmission electron microscopy (HAADF-STEM) was performed on the sample $Ba_{2.5}Sr_{0.5}NiSb_2O_9$ ($x = 0.5$) with a Themis Z G3 (Thermo Fisher Scientific) operated at 300 kV. This microscope is equipped with a Cs probe corrector (point resolution better than 60 pm) and a Super-X system (4 EDX detectors) allowing to

acquire elemental maps with atomic resolution. The powder was dispersed in ethanol (10 min in ultrasonic bath). A drop of this solution was deposited on a copper grid covered with a thin holey carbon film.

Commercial SQUID magnetometers (Quantum Design, MPMS) were used to collect dc magnetization data. Heat capacity measurements were performed in a multi-purpose device (Quantum Design, PPMS), using a semi-adiabatic relaxation technique coupled with a 2π analysis. To evaluate the lattice contribution in 3C $\text{Ba}_{1.75}\text{Sr}_{1.25}\text{NiSb}_2\text{O}_9$, the nonmagnetic isostructural compound 3C $\text{Ba}_{1.75}\text{Sr}_{1.25}\text{ZnSb}_2\text{O}_9$ was also investigated. This latter compound was synthesized in ceramic form by a solid-state reaction route similar to that used for preparing 3C $\text{Ba}_{1.75}\text{Sr}_{1.25}\text{NiSb}_2\text{O}_9$.

Muon spin relaxation (μSR) measurements were performed on the GPS and LTF instruments at the Paul Scherrer Institut and on the EMU spectrometer at the ISIS muon facility, in zero field (ZF) and longitudinal applied field (LF) geometries, down to 20 mK for 6H $\text{Ba}_{2.5}\text{Sr}_{0.5}\text{NiSb}_2\text{O}_9$ and 3C $\text{Ba}_{1.75}\text{Sr}_{1.25}\text{NiSb}_2\text{O}_9$. ^{121}Sb NMR experiments were performed for the 3C $\text{Ba}_{1.75}\text{Sr}_{1.25}\text{NiSb}_2\text{O}_9$ phase only, in the 1.2 – 60 K T-range, by sweeping the magnetic field in the $H = 5\text{--}7$ Teslas range at a 61.148 MHz fixed frequency and using a standard spin-echo technique.

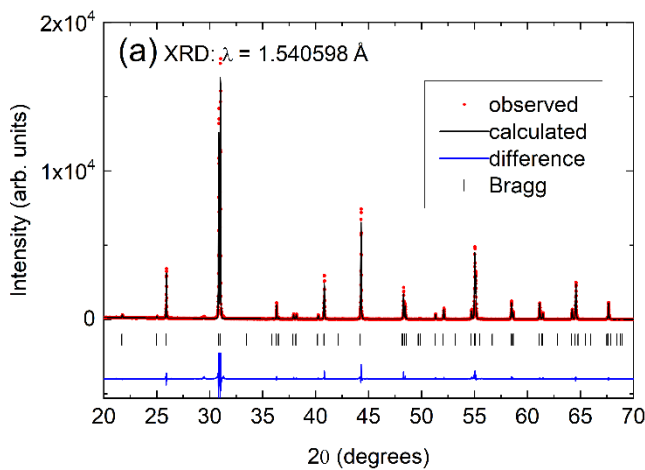
III. RESULTS

A. Crystal Structures

6H $\text{Ba}_{2.5}\text{Sr}_{0.5}\text{NiSb}_2\text{O}_9$ ($x = 0.5$)

The published $\text{P6}_3\text{mc}$ or $\text{P6}_3/\text{mmc}$ crystal structures of 6HB $\text{Ba}_3\text{NiSb}_2\text{O}_9$ produced during HP experiments [12,23] were used as starting models for combined refinements of our XRD and NPD data. Positions of the Bragg reflections are the same for both models. We first performed attempts with the non-centrosymmetric $\text{P6}_3\text{mc}$ model that was used for refining a powder XRD diffraction pattern of HP 6HB $\text{Ba}_3\text{NiSb}_2\text{O}_9$ [12]. Within this model, the NiSbO_9 pairs all have the same orientation (Fig. 1(a)). This $\text{P6}_3\text{mc}$ model failed to reproduce the observed intensities. Clear discrepancy between observed and calculated structure factors was obtained for several reflections. This result prompted us to test the alternating centrosymmetric $\text{P6}_3/\text{mmc}$ model with only one crystallographic Wyckoff 4f position and mixed Ni/Sb

occupancy for the two octahedral sites of a face-sharing bi-octahedra. A mirror plane at $z = 1/4$, which is absent in space group $P6_3mc$, passes through the common triangular face of the bi-octahedra. This causes a difference in structure factors and thus in reflection intensities between $P6_3mc$ and $P6_3/mmc$ models. For our powder sample of $Ba_{2.5}Sr_{0.5}NiSb_2O_9$, the $P6_3/mmc$ model led to a satisfactory level of agreement between observed and calculated patterns. Fig. 3 presents the final Rietveld plots. Table I shows the refined structural parameters and final agreement factors. Selected bond distances are listed in Table II. Maximum and minimum electron densities in the difference Fourier map were 0.88 electron/ \AA^3 and -1.1 electron/ \AA^3 , respectively. Atomic coordinates and ADP were kept identical for Ba1 and Sr1, for Ba2 and Sr2, and for Sb1 and Ni1 atoms. Anisotropic ADP for Ba/Sr sites and isotropic ADP for the other sites were refined with full occupancies of all sites. Sr is located at both 2b and 4f Ba positions. There was no detectable Sb2/Ni1 site mixing. The two central sites of the pair of face-shared octahedra (Wyckoff 4f positions) are almost equally occupied by Ni and Sb atoms. The Ni-Sb distance of 2.66 \AA in the $NiSbO_9$ unit is close to the Ni-Sb distance that was determined for HP 6HB $Ba_3NiSb_2O_9$ from EXAFS data (2.68 \AA) [21]. Furthermore, the O1-O1 distance within the common triangular face of the bi-octahedra (2.72 \AA) is quite different from that observed for the Sb_2O_9 dimers in the AP 6HA form of $Ba_3NiSb_2O_9$ (2.59 \AA) [22]. Another important result is that atomic coordinates, equivalent isotropic ADP and mean bond distances compare well with those previously obtained from a satisfactory combined refinement of powder XRD and NPD data for the HP 6HB-like trigonal phase of $Ba_3NiSb_2O_9$ using the same centrosymmetric $P6_3/mmc$ starting model [23].



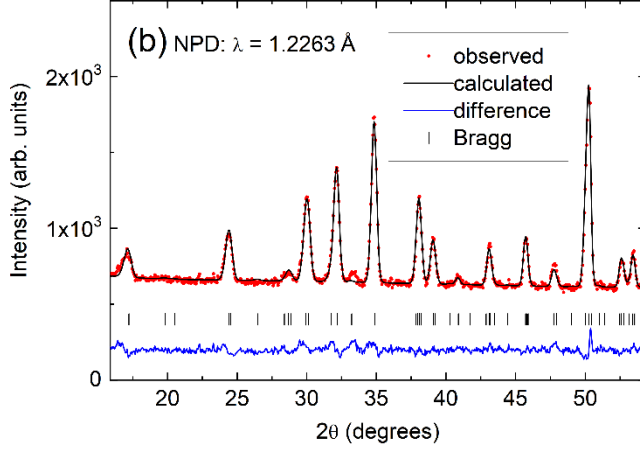


Figure 3. Final combined Rietveld refinement plots of the (a) XRD and (b) NPD data for $\text{Ba}_{2.5}\text{Sr}_{0.5}\text{NiSb}_2\text{O}_9$. Solid black curves are the best fits obtained with space group $\text{P6}_3/\text{mmc}$. The very weak Bragg reflections at $2\theta \approx 29.5^\circ$ (XRD) and 33° (NPD) were attributed to $\text{Ba}_3\text{SrSb}_2\text{O}_9$ impurity phase. Both portions of the observed diffraction profiles are shown for the same d -spacing range in order to illustrate that XRD and NPD data complement one another. Full patterns are shown in the Supplemental Material [30].

TABLE I. Refined structural parameters and final agreement factors for $\text{Ba}_{2.5}\text{Sr}_{0.5}\text{NiSb}_2\text{O}_9$ derived from X-ray and neutron diffraction data collected at 300 K^a. Combined refinements of X-ray and neutron diffraction data were performed with centrosymmetric space group $\text{P6}_3/\text{mmc}$.

Atom	Site	x	y	z	$U_{iso}(\text{\AA}^2)$	Occupancy
Ba1/Sr1	2b	0	0	1/4	0.0043(7)	Ba : 0.776(14)
						Sr : 0.224(14)
Ba2/Sr2	4f	1/3	2/3	0.09988(6)	0.0122(4)	Ba : 0.823(10)
						Sr : 0.177(10)
Sb2	2a	0	0	0	0.0044(1)	1
Sb1/Ni1	4f	1/3	2/3	0.65666(8)	0.0058(5)	Sb : 0.485(6)
						Ni : 0.515(6)
O1	6h	0.5094(4)	0.0189(8)	1/4	0.0148(7)	1
O2	12k	0.1630(4)	0.3259(7)	0.5797(1)	0.0129(5)	1

^a Space Group $P6_3/mmc$ (no. 194). Cell parameters: $a = 5.77206(2)$, $c = 14.24275(5)$. XRD: $GOF = 1.54$, $R_p = 9.51$, $wR_p = 13.52$. NPD: $GOF = 1.64$, $R_p = 2.30$, $wR_p = 2.89$. Over all: $GOF = 1.56$, $R_p = 5.74$, $wR_p = 6.16$.

TABLE II. Principal bond lengths (\AA) in $\text{Ba}_{2.5}\text{Sr}_{0.5}\text{NiSb}_2\text{O}_9$ derived from the joint refinement of X-ray and neutron diffraction data with space group $P6_3/mmc$. Mean bond distances reported for 6HB HP $\text{Ba}_3\text{NiSb}_2\text{O}_9$ in ref. [23] are given in parentheses.

Ba1/Sr1-O1 x4	2.888(3)	Sb2-O2 x4	1.986(3)
Ba1/Sr1-O1 x2	2.888(5)	Sb2-O2 x2	1.986(4)
Ba1/Sr1-O2 x6	2.922(3)	Mean Sb2-O2	1.986
Mean Ba1/Sr1-O	2.905		(1.985)
	(2.915)		
		Sb1/Ni1-O1 x2	2.059(3)
Ba2/Sr2-O1 x3	2.770(3)	Sb1/Ni1-O1 x1	2.059(4)
Ba2/Sr2-O2 x3	2.901(3)	Sb1/Ni1-O2 x2	2.025(3)
Ba2/Sr2-O2 x2	2.901(5)	Sb1/Ni1-O2 x1	2.025(4)
Ba2/Sr2-O2 x1	2.901(2)	Mean Sb1/Ni1-O	2.042
Ba2/Sr2-O2 x3	3.073(3)		(2.049)
Mean Ba2/Sr2-O	2.911		
	(2.922)	Sb1/Ni1- Sb1/Ni1	2.659(3)
			(2.72)

In order to get information with a different spatial resolution, we investigated the structure of $\text{Ba}_{2.5}\text{Sr}_{0.5}\text{NiSb}_2\text{O}_9$ using precession electron diffraction tomography (PEDT) on three different thin crystals harvested from the polycrystalline batch. The area probed by PEDT was about $200 \times 200 \text{ nm}^2$, as shown in Fig. 4. A detailed examination of PEDT patterns indicated a systematic absence of the odd-numbered $00l$ reflections. Although $00l$ odd reflections were observed on the $[010]$ PEDT pattern because of multiple diffraction, they disappeared by slightly tilting the crystals (Fig. 4(b)), indicating that the actual symmetry of these crystals of AP $\text{Ba}_{2.5}\text{Sr}_{0.5}\text{NiSb}_2\text{O}_9$ cannot be trigonal $P3m1$ or $P3$ as it was suggested for

HP 6HB $\text{Ba}_3\text{NiSb}_2\text{O}_9$ [23]. Our PEDT result stands in contrast to an earlier electron diffraction study of HP 6HB $\text{Ba}_3\text{NiSb}_2\text{O}_9$ which showed that its crystal structure cannot have hexagonal symmetry, although powder XRD and NPD patterns could be well refined in the hexagonal $\text{P6}_3/\text{mmc}$ triple-perovskite structure [23]. For $\text{Ba}_{2.5}\text{Sr}_{0.5}\text{NiSb}_2\text{O}_9$, refinements of the single-crystal PEDT intensities were conducted using the published $\text{P6}_3\text{mc}$ or $\text{P6}_3/\text{mmc}$ average structures of HP 6HB $\text{Ba}_3\text{NiSb}_2\text{O}_9$ as starting models [12,23]. Refined structural parameters and final agreement factors are given in the Supplemental Material [30] (see Tables 4, 5, and 6 in part A). While both refinements yielded reasonable and comparable agreement factors, the low ADP value of Ni1 (2b site) obtained with the non-centrosymmetric S.G. $\text{P6}_3\text{mc}$ suggests a mixed Ni/Sb occupation of each of the two octahedral sites of the dumbbell. Structural parameters obtained using the centrosymmetric $\text{P6}_3/\text{mmc}$ model are in good agreement with those derived from XRD and NPD data (Table I).

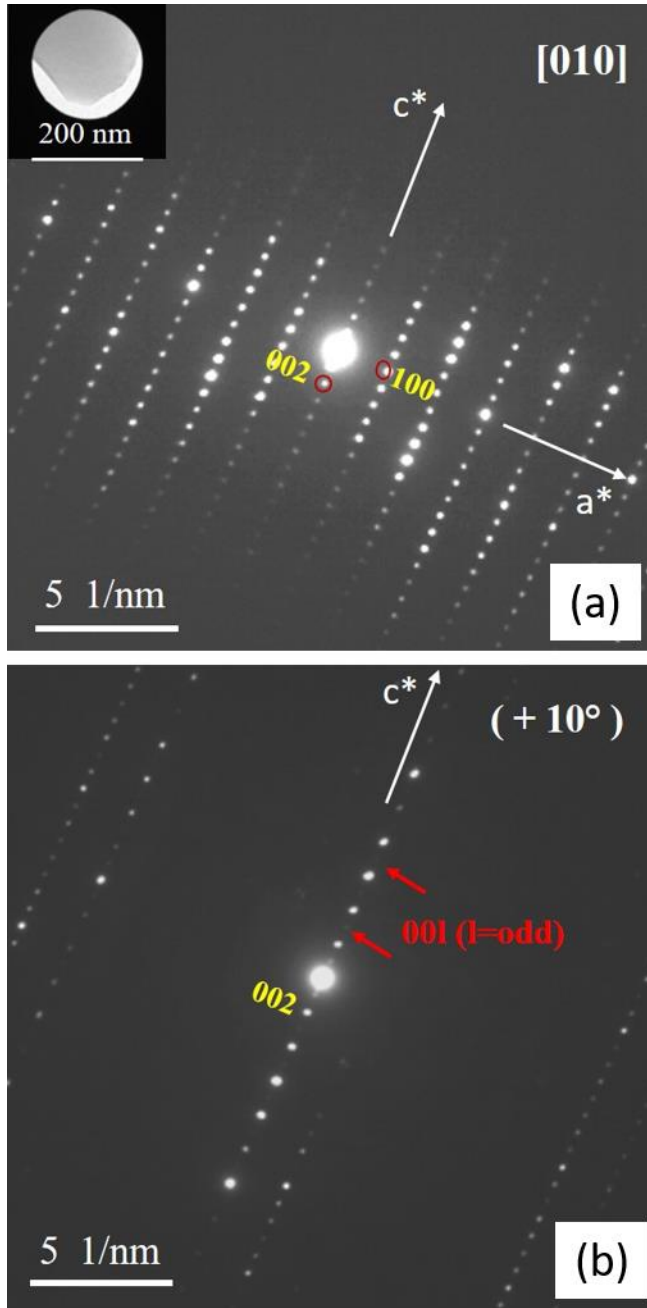


Figure 4. (a) [010] PEDT pattern for $\text{Ba}_{2.5}\text{Sr}_{0.5}\text{NiSb}_2\text{O}_9$. $00l$ -odd reflections are observed because multiple diffraction. Probed area is shown as an inset. (b) Tilted PEDT pattern (10° around c^*). Odd-numbered $00l$ reflections are missing.

Finally, $\text{Ba}_{2.5}\text{Sr}_{0.5}\text{NiSb}_2\text{O}_9$ was investigated by HAADF-STEM and EDX mapping (Fig. 5). An HAADF image viewed along the [010] axis is shown in Fig. 5(a). The intensity of HAADF images is a function of both the atomic number Z , approaching a Z^2 Rutherford-like relationship, and the projected thickness. Considering that the thickness does not vary

significantly at such a scale, projections of the columns with the heavier atoms will appear brighter. This allowed us to superimpose the projection of the $P6_3/mmc$ structure derived from the joint refinement of X-ray and neutron diffraction data. In order to confirm the identification of the columns, EDX mapping was acquired for ~ 40 min. Elemental maps of Ba, Ni and Sb are presented in Fig. 5(b), (c) and (d). It is clear that columns containing Ni atoms also contain Sb atoms (see orange ovals), and that intensity of columns containing only Sb atoms is much higher than those with both Sb and Ni. A net intensity profile performed in a direction perpendicular to three adjacent columns containing Sb atoms evidenced that brighter columns are twice as intense as the other ones (Fig. 5(e)). This is consistent with site occupancies obtained from the $P6_3/mmc$ refinement of X-ray and neutron powder diffraction data (Table I): 1 for Sb on 2a site, 48/52 for Sb/Ni on 4f site of the $NiSbO_9$ bi-octahedra. In other words, each column of 4f sites along the b-axis contains roughly the same number of Ni and Sb atoms. As a consequence, we did not observe a fully ordered “all-up” arrangement for the Ni-Sb dumbbells at the length scale of the crystal thickness along the [010] direction. For this direction of projection, it is however not possible to distinguish between complete disorder with random orientation of the dumbbells and a superimposition of several nanosized domains with nanoscale order in the orientation of the Ni-Sb dumbbells.

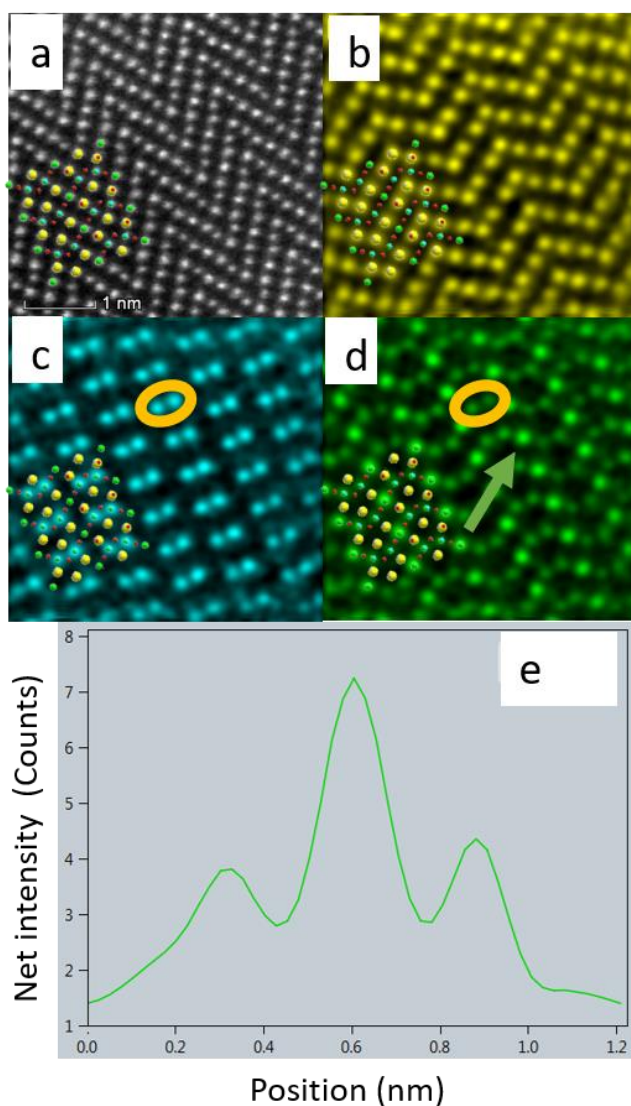


Figure 5. HAADF-STEM and EDX mapping for $\text{Ba}_{2.5}\text{Sr}_{0.5}\text{NiSb}_2\text{O}_9$ along the b-axis with projections of the $\text{P6}_3/\text{mmc}$ structure derived from powder XRD and NPD. (a) HAADF-STEM image (20 mrad convergence angle, 91 mm camera length, 63-200 mrad collection angle range). (b, c, d) EDX maps of Ba, Ni, and Sb, respectively. Maps were obtained after Gaussian blur pre filtering and Radial Wiener post-filtering with Velox software, Thermo Scientific. (e) Net intensity profile along the green arrow shown on the Sb map.

Several conclusions can be drawn from all these results. Judging from powder XRD and NPD, AP $\text{Ba}_{2.5}\text{Sr}_{0.5}\text{NiSb}_2\text{O}_9$ and HP 6HB $\text{Ba}_3\text{NiSb}_2\text{O}_9$ have very similar average structures that are typical of a hexagonal triple-perovskite containing NiSbO_9 face-sharing bi-octahedra (6HB phase). Their actual structures could however differ in terms of Ni-Sb dumbbell arrangement, which is different from the “all up” long range order depicted in Fig. 1(a) in both cases. Successful refinements of both our powder diffraction patterns and our PEDT data with the

centrosymmetric $P6_3/mmc$ model strongly suggest the absence of long-range order for the Ni-Sb dumbbell arrangement. We note in passing that the same $P6_3/mmc$ structural model also provided description of the average room temperature crystal structures of AP $Ba_3CuSb_2O_9$ based on single crystal X-ray diffraction data with Cu/Sb ratio at the 4f position equal to unity [10]. For this latter compound, which contains Jahn-Teller active Cu^{2+} ions, further investigations indicated nanoscale Cu-Sb dumbbell honeycomblike ordering [10,20]. In HP 6HB $Ba_3NiSb_2O_9$, it was suggested that polycrystalline samples contain ordered domains of small dimensions (1-10 nm) having a trigonal structure like the one shown in Fig. 1(b) without the 6_3 axis and the c glide plane of the $P6_3/mmc$ hexagonal unit cell [23]. In this scenario, Rietveld refinements of XRD and NPD patterns gives a centrosymmetric $P6_3/mmc$ average structure over many domains. These domains were not observed in the HAADF-STEM image obtained along the b-axis for HP 6HB $Ba_3NiSb_2O_9$ and it was therefore assumed that this image was obtained from a crystallite that contain several domains throughout its thickness [23]. Even if we did not observe neither the trigonal symmetry in thin crystals nor regions with co-aligned dumbbells on our HAADF-STEM images projected along the b-axis, chemical correlations for the Ni-Sb dumbbell arrangement may exist in our samples of $Ba_{2.5}Sr_{0.5}NiSb_2O_9$, too. Such chemical correlations would however be different in nature from those suggested for HP 6HB $Ba_3NiSb_2O_9$ because the trigonal symmetry, which is compatible with up-down-up-down correlations for the dumbbell arrangement along the stacking c axis, was not observed in thin crystals of $Ba_{2.5}Sr_{0.5}NiSb_2O_9$.

3C $Ba_{1.75}Sr_{1.25}NiSb_2O_9$ ($x = 1.25$)

Table III shows the refined structural parameters and final reliability factors obtained for $Ba_{1.75}Sr_{1.25}NiSb_2O_9$. Our starting point for the structure refinement was the published $Fm\bar{3}m$ crystal structure of the 3C HP phase of $Ba_3NiSb_2O_9$ [12]. Within this model, a $Ba_{3-x}Sr_xNiSb_2O_9$ structure is described as a $(Ba,Sr)_2BB'O_6$ double perovskite ($Ba_{(6-2x)/3}Sr_{2x/3}Ni_{2/3}Sb_{4/3}O_6$) where B and B' octahedral sites are occupied by Sb and $(2/3Ni + 1/3Sb)$ atoms, respectively (Fig. 2). Ni and Sb atoms are randomly distributed at the B' site [12]. Rock salt ordering of B/B' cations is actually a common occurrence in $A_2BB'O_6$ double perovskite [34,35]. Using this starting model, a satisfactory combined refinement of our XRD and NPD data was obtained. Maximum and minimum electron densities in the difference Fourier map were 0.74 and -0.38 electron \AA^{-3} , respectively. Fig. 6 shows the final Rietveld plots. There was no sign of additional structural

periodicities. Atomic coordinates and isotropic ADP were kept identical for Ba and Sr atoms at Wyckoff 8c site, and for Ni and Sb atoms at Wyckoff 4b site. Crystallographic sites were all assumed to be fully occupied and site occupancies were refined for the Ba/Sr(8c) and Ni/Sb(4b) sites. It yielded cationic ratios close to the nominal ones; Sr/Ba \approx 0.66(2) (versus nominal 0.71) and Ni/Sb \approx 1.92(3) at 4b site (versus nominal 2.0). The only refined atomic coordinate, namely $x = 0.2533(1)$ for O atom at Wyckoff 24e position, is close to the one determined from powder XRD data for HP 3C Ba₃NiSb₂O₉, $x = 0.2409(8)$ [12]. The mean Sb-O bond length around the 4a site, 1.9928(9) Å, is close to the values reported for the SbO₆ octahedron in the double perovskite structure of Sr₃NiSb₂O₉ (1.99-2.01 Å) [36,37]. The latter compound ($x = 3$) is prepared at AP using a high-temperature solid state reaction method similar to that used for Ba_{1.75}Sr_{1.25}NiSb₂O₉. The mean Ni/Sb-O bond distance around the 4b site is 2.0454(9) Å, which is similar to the values of 2.03 Å found for the (Ni_{2/3}Sb_{1/3})O₆ octahedron in Sr₃NiSb₂O₉ [37]. The mean Ba/Sr-O bond length of 2.85556(2) Å compares well with both the mean Sr-O distance of 2.82 Å observed in Sr₃NiSb₂O₉ [37] and the Ba-O distance calculated from ionic radii (3.01 Å).

TABLE III. Refined structural parameters and final agreement factors for 3C Ba_{1.75}Sr_{1.25}NiSb₂O₉ derived from X-ray and neutron diffraction data collected at 300 K.^a Refinements were performed using a $Fm\bar{3}m$ double perovskite in a A₂BB'O₆ model with A(8c) = Ba_{0.583}Sr_{0.417}, B(4a) = Sb and B'(4b) = Ni_{2/3}Sb_{1/3} as a starting model.

Atom	Site	x	y	z	$U_{iso}(\text{\AA}^2)$	Occupancy
Ba/Sr	8c	1/4	1/4	1/4	0.0104(1)	Ba: 0.601(5) Sr: 0.399(5)
Sb	4a	1/2	1/2	1/2	0.0032(2)	1
Ni/Sb	4b	0	0	0	0.0031(2)	Ni: 0.658(3) Sb: 0.342(3)
O	24e	0.2533(1)	0	0	0.01262(7)	1

^aSpace Group: $Fm\bar{3}m$ (no. 225). Cell parameter: $a = 8.07640(3)$. XRD: GOF = 1.42, $R_p = 9.12$, $wR_p = 14.14$. NPD: GOF = 3.76, $R_p = 3.39$, $wR_p = 4.57$. Over all: GOF = 1.99, $R_p = 4.86$, $wR_p = 5.82$.

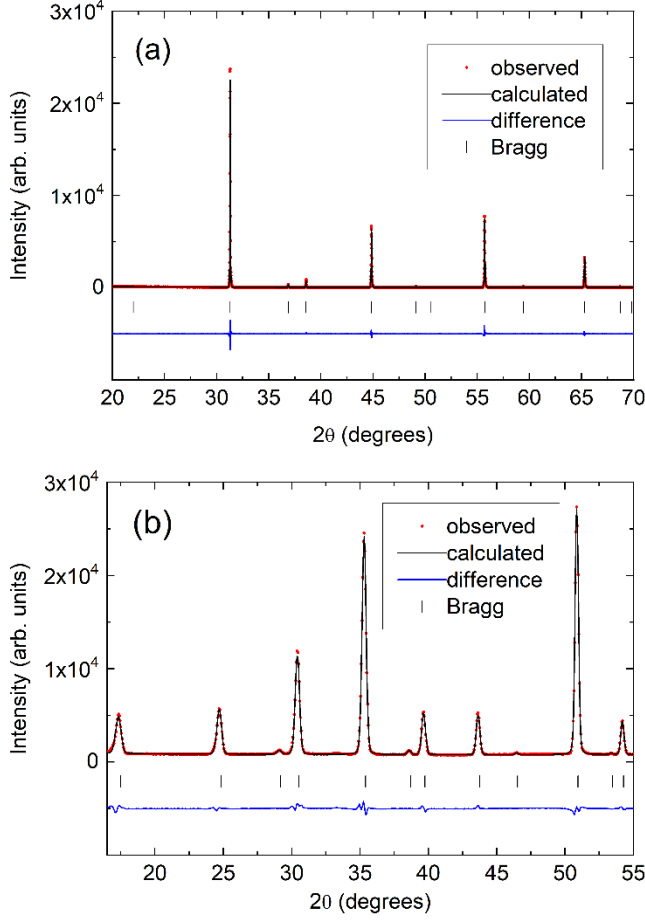


Figure 6. Final combined Rietveld refinement plots of the (a) XRD ($\lambda = 1.540598 \text{ \AA}$) and (b) NPD data ($\lambda = 1.2247 \text{ \AA}$) for 3C $\text{Ba}_{1.75}\text{Sr}_{1.25}\text{NiSb}_2\text{O}_9$. Both portions of the observed diffraction profiles are shown for the same d -spacing range in order to illustrate that XRD and NPD data complement one another. Full patterns are shown in the Supplementary Material.

B. Magnetization and Heat Capacity

Fig. 7 shows the temperature dependent magnetic susceptibility, $\chi(T)$, of 6H $\text{Ba}_{2.5}\text{Sr}_{0.5}\text{NiSb}_2\text{O}_9$ and of 3C $\text{Ba}_{1.75}\text{Sr}_{1.25}\text{NiSb}_2\text{O}_9$. These two phases will be hereafter referred to as 6H-Sr and 3C-Sr, respectively. Previously obtained data for 6HB and 3C phases of pure $\text{Ba}_3\text{NiSb}_2\text{O}_9$ [12,24] synthesized under HP, termed 6HB-HP and 3C-HP below, are also shown in Fig. 7(a) for comparison. The Weiss temperatures and effective moments as extracted from the high- T plot of χ^{-1} versus T are listed in Table IV. The Weiss temperatures of the 6H-Sr ($\Theta_{\text{Weiss}} \approx -65 \text{ K}$) and of 3C-Sr ($\Theta_{\text{Weiss}} \approx -213 \text{ K}$) phases reflect dominant antiferromagnetic spin-

spin interactions whose magnitudes are similar to those observed in the HP phases of pure $\text{Ba}_3\text{NiSb}_2\text{O}_9$.

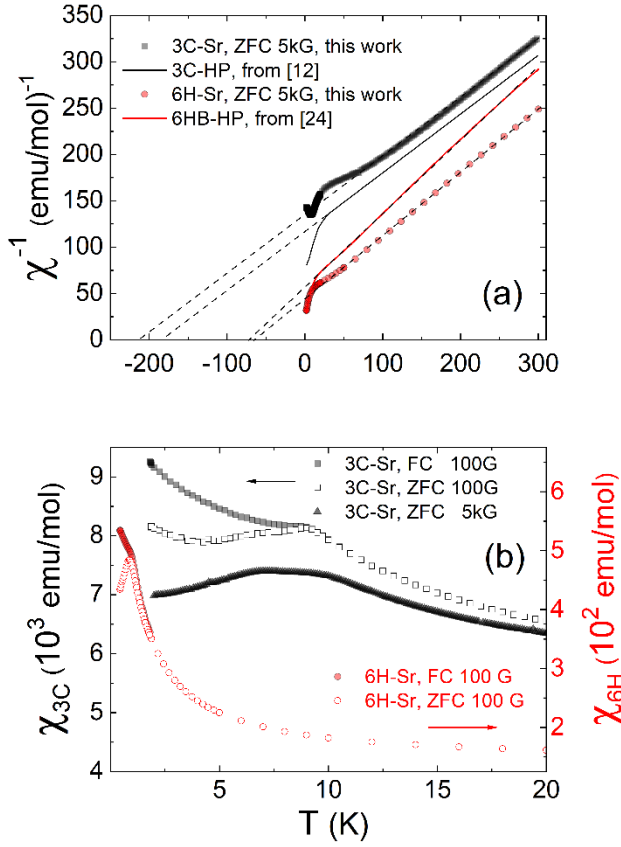


Figure 7. (a) Inverse magnetic susceptibility χ^{-1} versus temperature T for our samples of $\text{Ba}_{2.5}\text{Sr}_{0.5}\text{NiSb}_2\text{O}_9$ (“6H-Sr”) and of $\text{Ba}_{1.75}\text{Sr}_{1.25}\text{NiSb}_2\text{O}_9$ (“3C-Sr”), compared to 6HB and 3C phases of $\text{Ba}_3\text{NiSb}_2\text{O}_9$ synthesized under high pressure (“6HB-HP” and “3C-HP”) [12,24]. (b) Low- T susceptibility of 6H-Sr and 3C-Sr samples.

TABLE IV. Values of the effective Ni moments and Weiss temperatures for 6H $\text{Ba}_{2.5}\text{Sr}_{0.5}\text{NiSb}_2\text{O}_9$ (“6H-Sr”) and 3C $\text{Ba}_{1.75}\text{Sr}_{1.25}\text{NiSb}_2\text{O}_9$ (“3C-Sr”), compared to existing data for the phases of pure $\text{Ba}_3\text{NiSb}_2\text{O}_9$ obtained under high pressure (“6HB-HP” and “3C-HP”).

Phase	Synthesis	μ_{eff} (μ_{B}/Ni)	Θ_{Weiss} (K)	Reference
6H	6HB-HP	~ 3.54	-75.6(6)	[12]
		3.29(2)	- 73(2)	[24]
	6H-Sr	3.43(2)	- 65(1)	This work
3C	3C-HP	~ 3.54	-182.5(3)	[12]
	3C-Sr	3.55 (2)	- 213(2)	This work

For the 6HB-HP phase of $\text{Ba}_3\text{NiSb}_2\text{O}_9$, no FC-ZFC splitting was observed for the susceptibility measured under a field of 5 kG down to 2 K [12]. We know of no ZFC-FC data acquired under a lower field value for 6HB-HP. A spin liquid behavior was confirmed through μSR and NMR experiments, with a levelling off of the local susceptibility below 50 K as measured through the shift of the ^{121}Sb NMR line [24]. The upturn in ZFC- $\chi(T)$ measured at 5 kG or 1 kG was analyzed by introducing an additional Curie component corresponding to a $\sim 2\%$ of $S = 1$ orphan spins [12,24]. The variable-temperature ZFC magnetic susceptibility measured at 5 kG for 6H-Sr $\text{Ba}_{2.5}\text{Sr}_{0.5}\text{NiSb}_2\text{O}_9$ is comparable to the published data for 6HB-HP, showing a similar Curie tail at low temperature. For an applied field of 100 G, the 6H-Sr compound displays a clear opening between the ZFC and FC branches at 0.95(15) K and a maximum in the ZFC trace (Fig. 7(b)). μSR experiments described in the next section show, however, that this opening does not arise from a bulk magnetic transition, e.g., a spin-glass transition. As can be seen in Fig. 8, magnetization measurements performed at 0.450 K can be analyzed using a combination of a non-saturated linear term and a term corresponding to $\sim 2\%$ orphan spins, similarly as in the 6HB-HP phase.

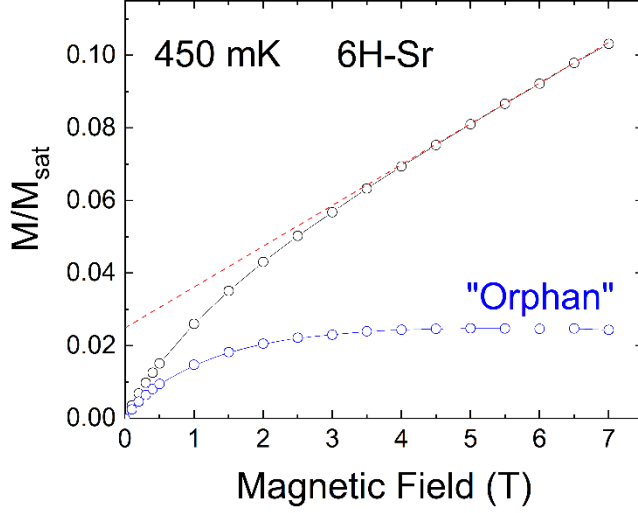


Figure 8. Magnetization M plotted as M/M_{sat} versus applied field at 450 mK for $\text{Ba}_{2.5}\text{Sr}_{0.5}\text{NiSb}_2\text{O}_9$ (“6H-Sr”). The saturation magnetization $M_{\text{sat}} \propto g S \mu_B$ was calculated using $S = 1$ and $g = 2.4$. The fit (red line) is the combination of a linear term and a Brillouin function for a spin 1 (“Orphan” contribution).

For the 3C phases, our susceptibility results for 3C-Sr $\text{Ba}_{1.75}\text{Sr}_{1.25}\text{NiSb}_2\text{O}_9$ show a low- T behavior which differs notably from that reported in ref. [12] for 3C-HP $\text{Ba}_3\text{NiSb}_2\text{O}_9$. The zero-field-cooled susceptibility curve $\chi(T)$ measured under a field of 5 kG displays two changes of slope at about 10 and 6 K (Fig. 7(b)), which were absent in 3C-HP $\text{Ba}_3\text{NiSb}_2\text{O}_9$. Furthermore, a FC-ZFC bifurcation occurs in the susceptibility data below 9 K for applied fields up to 10 kG, combined with a sample dependent small Curie upturn of the susceptibility. To provide further insight, the magnetic specific heat, $C_M(T)$, of 3C-Sr $\text{Ba}_{1.75}\text{Sr}_{1.25}\text{NiSb}_2\text{O}_9$ was also measured. It features a broad maximum at 12 K as shown in Fig. 9, slightly higher than both the FC-ZFC splitting and the changes of slope in the susceptibility curves. Our C_M/T data substantially differs from the data for 3C-HP $\text{Ba}_3\text{NiSb}_2\text{O}_9$ from ref. [12], for which a broad maximum was also reported but at a lower temperature of ~ 8 K. The magnetic total entropy is also found larger here, 40% instead of 22% of $R\ln(3)$ per $S = 1$ spin. At low- T , between 2 and 7 K, a quadratic behavior of the specific heat is found, $C_M \sim 1.7 \cdot 10^{-2} T^2$ J/mol K. A similar quadratic behavior of $C_M(T)$ was observed for 3C-HP $\text{Ba}_3\text{NiSb}_2\text{O}_9$ between 0.35 and 5 K but with a larger slope.

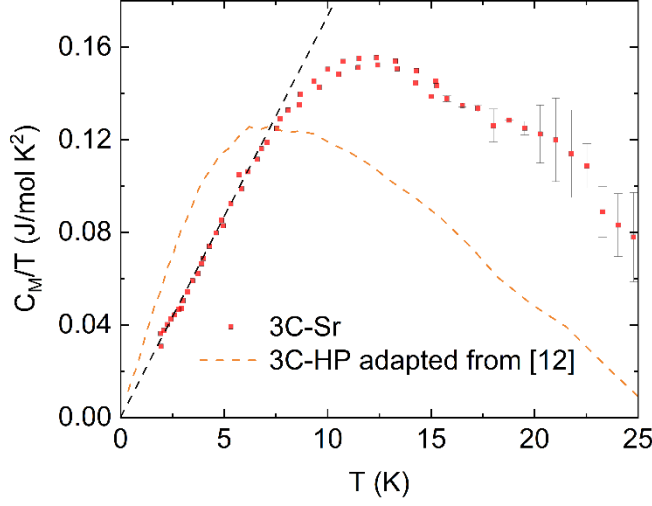


Figure 9. Magnetic specific heat plotted as C_M/T versus temperature T for $\text{Ba}_{1.75}\text{Sr}_{1.25}\text{NiSb}_2\text{O}_9$ (“3C-Sr”). The straight dashed line is the fit $C_M = \gamma T^2$ with $\gamma \sim 1.7 \cdot 10^{-2} \text{ J/mol K}^3$. The dashed curve represents the results from [12] for the 3C-HP phase of $\text{Ba}_3\text{NiSb}_2\text{O}_9$ synthesized under high pressure.

C. Muon Spin Relaxation (μSR) and ^{121}Sb NMR

In order to reveal the intrinsic properties of the two new 6H-Sr and 3C-Sr phases, we have further performed local probe μSR and NMR experiments.

3C Ba_{1.75}Sr_{1.25}NiSb₂O₉ (“3C-Sr”)

We performed both μSR and NMR measurements on the very same sample of the 3C-Sr phase, and they gave a consistent picture as detailed below. Fig. 10 shows the muon decay asymmetry in zero field for different temperatures down to 1.6 K. The dramatic increase of the early time relaxation rate around 11 K, together with the larger weight of the long-time tail at low temperature, are typical signatures of a magnetic transition from paramagnetism to static magnetism in the ground state. Accordingly,

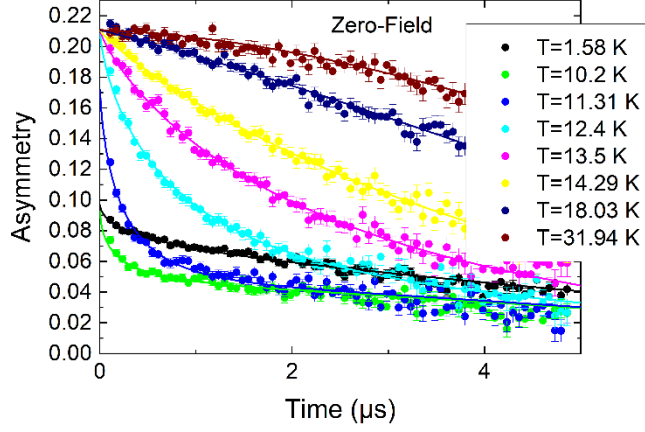


Figure 10. Muon decay asymmetry in zero applied field in 3C Ba_{1.75}Sr_{1.25}NiSb₂O₉ (3C-Sr). Lines are fits described in the text.

the asymmetry at long time $t > 0.1\mu\text{s}$ could be fitted on the whole T range to

$$a(t) = (a_0 - a_p) \left((1 - f) e^{-(\sigma t)^2} e^{-(\lambda t)^\beta} + \frac{f}{3} e^{-(\lambda_f t)^{1/2}} \right) + a_p e^{-(\sigma t)^2} e^{-\lambda_p t}$$

where $a_0 = 0.21$ is the initial asymmetry, $a_p/a_0 = 0.2$ is a fraction of the muon sites which do not sense any frozen field, e.g. surrounded by Sb's only and is kept unchanged at all temperatures. The fraction f stands for the volume fraction of the 3C-Sr phase that undergoes the magnetic transition. Above 12.4 K f is set to 0 and the relaxation is both due to static nuclear moments, yielding the gaussian decay term ($\sigma = 0.11 \mu\text{s}^{-1}$), and fluctuations of the electronic moments, yielding the roughly exponential decay term $e^{-(\lambda t)^\beta}$ ($0.7 < \beta < 1$). The relaxation rate λ increases gradually as shown in Fig. 11 upon cooling towards the magnetic transition temperature. Below 10.2 K f could be set to 1, i.e. static magnetism has developed in the whole sample volume except for the a_p fraction. In the $t > 0.1\mu\text{s}$ time window shown, only the slow relaxation of the expected 1/3rd tail, corresponding to muon spins aligned with the internal fields, is detected while the fast relaxing 2/3rd component of the frozen signal is missing (this component is discussed further below). The exponent 1/2 of the stretched exponential relaxation $e^{-(\lambda_f t)^{1/2}}$ in this regime points to a wide distribution of relaxation rates and the possibility of a disordered ground state. Close to the transition, for $T = 11.3$ K, both static and dynamical fractions contribute and the best fit to the data gives $f = 0.30(1)$. The relaxation rate shows a well-defined but rather broad peak around 8.5(5) K, substantially below the magnetic transition 11(1) K temperature, suggesting unusual magnetic excitations.

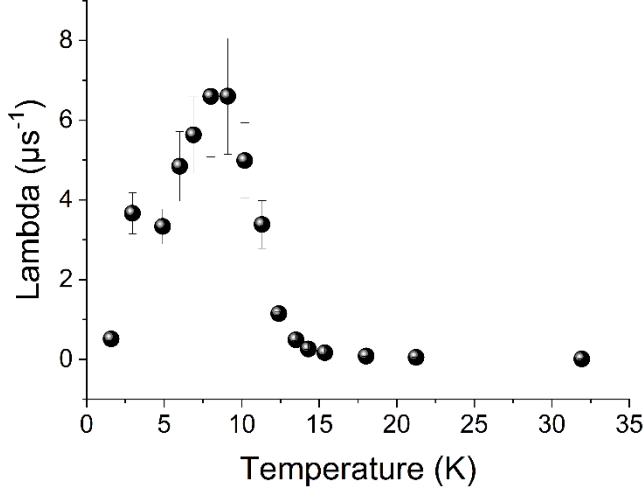


Figure 11. Temperature evolution of the relaxation rate in 3C Ba_{1.75}Sr_{1.25}NiSb₂O₉. The plotted rate is λ above 12.4 K, λ_f below 10.2 K and a weighted average $f\lambda_f + (1-f)\lambda$ at $T = 11.3$ K.

The early time relaxation ($t < 0.25 \mu\text{s}$) is presented at various temperatures below the transition on Fig. 12. A strongly damped spontaneous oscillation in zero applied field is clearly visible at low temperature which discards a spin-glass scenario where only one dip in the asymmetry would be expected. It gives evidence for a magnetically long range ordered ground state albeit with substantial disorder in line with the square root exponential relaxation discussed above in the same T range. The early time relaxation was fitted to

$$a(t) = a_s \left(\frac{1}{3} + \frac{2}{3} \cos(2\pi\nu_s t + \varphi) e^{-(\sigma_s t)^2} \right) e^{-\lambda_{osc} t} + a_b \left(\frac{1}{3} + \frac{2}{3} e^{-(\sigma_b t)^2} \right) e^{-\lambda_b t} + a_p$$

with the constraint $a_s + a_b + a_p = a_0$. The second term accounts for the initial gaussian like relaxation, likely arising from too fast and too damped oscillations to be detected. The first oscillating term gives the frequency ν_s of the spontaneous oscillation which is plotted in the right panel of Fig. 12. The precession of the muon spin in zero field is a direct signature of the presence of an internal field $B_{int} = 2\pi\nu_s/\gamma$ at the muon stopping where $\frac{\gamma}{2\pi} = 135.5 \text{ MHz/T}$ is the muon gyromagnetic ratio. Therefore $\nu_s(T)$ represents the order parameter in the magnetic phase.

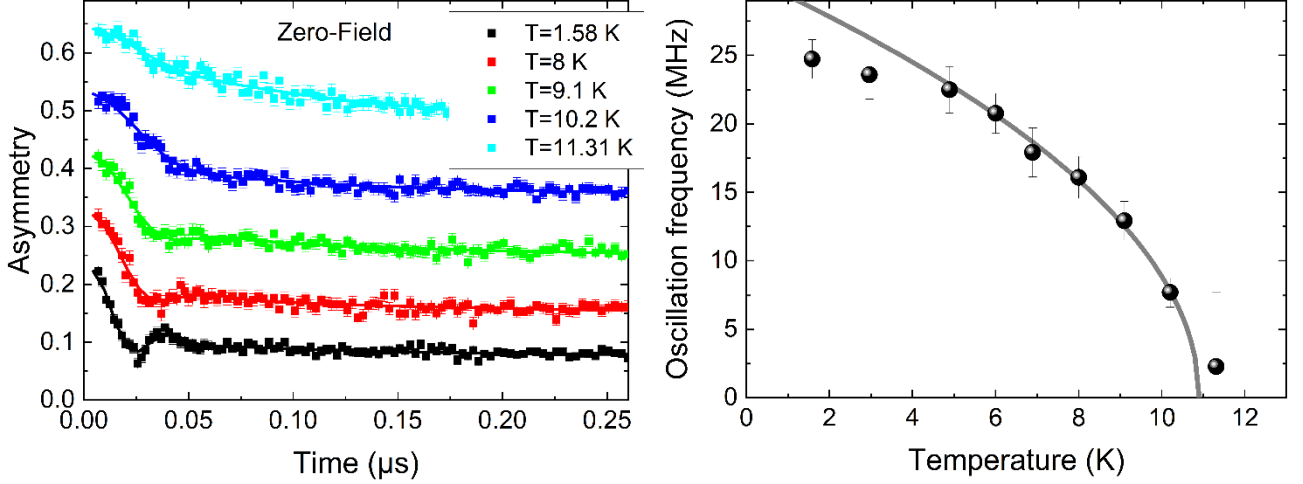


Figure 12. Left: Early time muon decay asymmetry in zero field in 3C Ba_{1.75}Sr_{1.25}NiSb₂O₉ (3C-Sr) at selected temperatures below the transition. For clarity, the spectra are shifted vertically by $\Delta a = 0.1$ from each other. Lines are fits described in the text. Right: temperature evolution of the damped oscillation frequency extracted from the fits in the left panel. The line is a plot of $A\sqrt{1 - T/T_N}$ with $A = 30.8$ MHz and $T_N = 10.9$ K.

We now detail our ^{121}Sb NMR measurements which confirm the presence of a static ordering below 11(1) K. In Fig. 13(c), some typical spectra taken in the 1.2 – 60 K range are displayed for the 3C-Sr sample. A progressive broadening occurs as reported in Fig. 13(b) with decreasing temperatures in the T -range 60-12 K. It is the hallmark of a distribution of local fields which can be either assigned to a distribution of Ni susceptibilities or a distribution of hyperfine couplings of the ^{121}Sb nuclei to the surrounding Ni's. Most strikingly, the intensity of our signal dramatically decreases around 10 K where a marked kink occurs in the susceptibility data (Fig. 13(a)) taken under a 5 kG field. The loss of intensity results from a distribution of relaxation times, a large part of which becomes shorter than the 10 μs lower limit of the NMR time window [38,39]. This increase of the transverse relaxation rate can be safely assigned to a slowing down of the fluctuations in the context of a phase transition, also evident through the $1/T_1$ divergence (Fig. 13(d)).

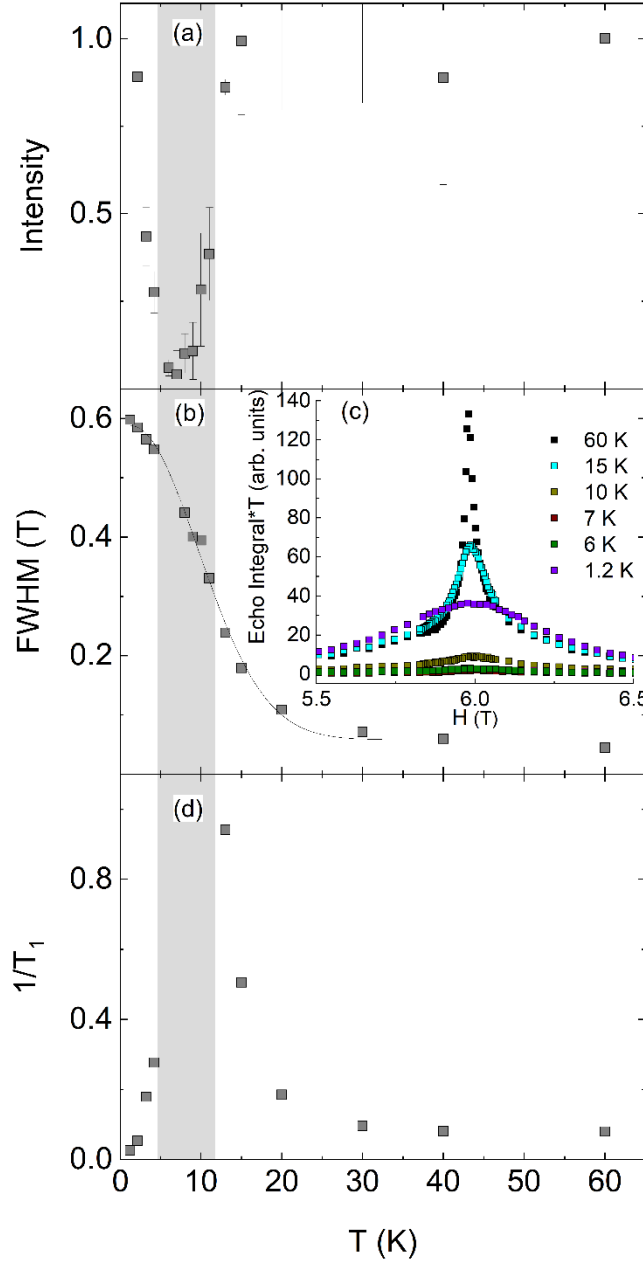


Figure 13. ^{121}Sb NMR data for $3\text{C Ba}_{1.75}\text{Sr}_{1.25}\text{NiSb}_2\text{O}_9$: (a) Integrated spectral intensity corrected by T_2 relaxation effects: it represents the normalized number of detected nuclei. The grey area signals the T -range where only a weak intensity is detected, therefore the NMR spectra reflect only a minority of sites harboring the longest T_2 's. (b) Full width measured at half maximum for all spectra from 60 to 1.2 K (c) Plot of typical ^{121}Sb NMR spectra obtained by sweeping the field at a fixed frequency of 61.148 MHz. The signal is hardly observable around 10 K. (d) Divergence of the longitudinal relaxation rate $1/T_1$ signaling a magnetic transition.

From the scaling of the shift with the susceptibility between 80 and 300 K (not shown), we could extract a hyperfine constant of 3.43 (10) kOe/ μ_B . In the case of a perfect ordering with a well-defined value of the internal field in a powder sample, one expects a rectangular lineshape, with a full width equal to twice the internal field at the Sb site. On the contrary, the lineshape observed here has a Lorentzian shape, reflecting a distribution of internal fields and thus a substantial amount of disorder in the frozen phase. The half width at half maximum of 0.3 T indicates a subsequent freezing with a moment value of 0.87(3) μ_B . This is also in line with the low value of $1/T_1$ found in our relaxation measurements at 1.2 K showing that there is no or very little persistent fluctuations as expected for conventional magnetic phases. All these results perfectly match the μ SR results.

6H Ba_{2.5}Sr_{0.5}NiSb₂O₉ (6H-Sr)

For the 6H-Sr phase, the NMR transverse relaxation times T_2 's are extremely short, which prohibits the drawing of firm conclusions as discussed in ref. [24] for the 6HB-HP phase of Ba₃SrNiSb₂O₉, especially at low- T , which is our main focus here.

The μ SR relaxation measured in a powder sample of the 6H-Sr compound is in marked contrast to the 3C-Sr case described above. Although an increase of the relaxation rate is similarly observed upon cooling the sample, it remains moderate and nearly T -independent below 1 K. Note also that, at variance with the 3C-Sr case, there is no crossing of the asymmetry curves, thus no development of a $1/3^{\text{rd}}$ tail at low temperature, which would be characteristic of the presence of static internal fields. This discards a spin-glass ground state and suggests a dynamical behaviour of the 6H-Sr phase across the whole temperature range, down to 95 mK, the lowest temperature of this study. This was also the case in the 6HB-HP pure compound [24]. Therefore, the absence of static magnetism at $T \rightarrow 0$ K, a first hint at a spin liquid ground state, seems to be a robust feature of the 6H phases having Ni-Sb dumbbells, whatever the synthesis route used to stabilize it. There are nonetheless interesting differences in muon spin relaxation between the 6HB-HP and 6H-Sr materials that we investigate below in details.

At variance with the 6HB-HP counterpart where the relaxation remains exponential at all temperatures, there is a clear evolution in the form of the μ SR signal in the 6H-Sr sample from exponential at high temperatures to Gaussian at low T (see Fig. 14, left). In the usual Dynamical

Kubo-Toyabe (DKT) model [40], the Gaussian shape at low T implies very slow fluctuations at the verge of static magnetism. To quantify this effect, we fitted the relaxations to

$$a(t) = a_0 G(t, \nu, \Delta, B_L) + a_{bkg}$$

where $G(t, \nu, \Delta, B_L)$ is the function introduced in [41] to approximate the DKT model in the fluctuating regime, i.e. as long as the fluctuation frequency ν is larger than the width of the distribution of fluctuating internal fields, Δ . We could get reasonable fits of the data at all temperature with this model function with no applied field and with ν as the only variable parameter. The temperature evolution of ν is shown in the inset of Fig. 15. As expected from the shape of the relaxation, the fluctuations slow down drastically, by about 2 orders of magnitude, from high to low T . At base T , $\nu/\Delta \sim 1.6$ which is indeed close to static magnetism ($\nu/\Delta = 1$). For such slow fluctuations, we expect that a longitudinal field $B_L \gg \Delta/\gamma = 9.2(1)$ G applied along the initial muon spin direction should dominate the total field probed by the muons and suppress the relaxation as shown by the simulations in the right panel of Fig. 14 for $B_L = 0.05$ T and 0.4 T respectively. However, for such applied fields, the experimental relaxation remains surprisingly large, pointing to much stronger spin fluctuations than anticipated from the Gaussian relaxation shape. Such an ‘undecouplable’ Gaussian shape, observed previously in some highly frustrated magnets [42–44] remains mysterious to date but certainly suggests exotic spin dynamics in this $S = 1$ triangular compound.

To compare with the zero field relaxation rate obtained in the 6HB-HP pure counterpart from exponential fits [24], we used the fast fluctuation approximation $G(t, \nu, \Delta, B_L = 0) \simeq e^{-2\Delta^2 t/\nu}$ and we plotted $\lambda = 2\Delta^2/\nu$ for the 6H-Sr case in Figure 15. The slowing down of the spin fluctuations in the 6H-Sr compound shifted to a significantly lower temperature (typically 2.4 times lower) than in the 6HB-HP pure one. We note that this difference cannot be explained by the much smaller change in the magnetic interactions in the two variants. Indeed, both compounds show similar Curie-Weiss temperatures (see table IV).

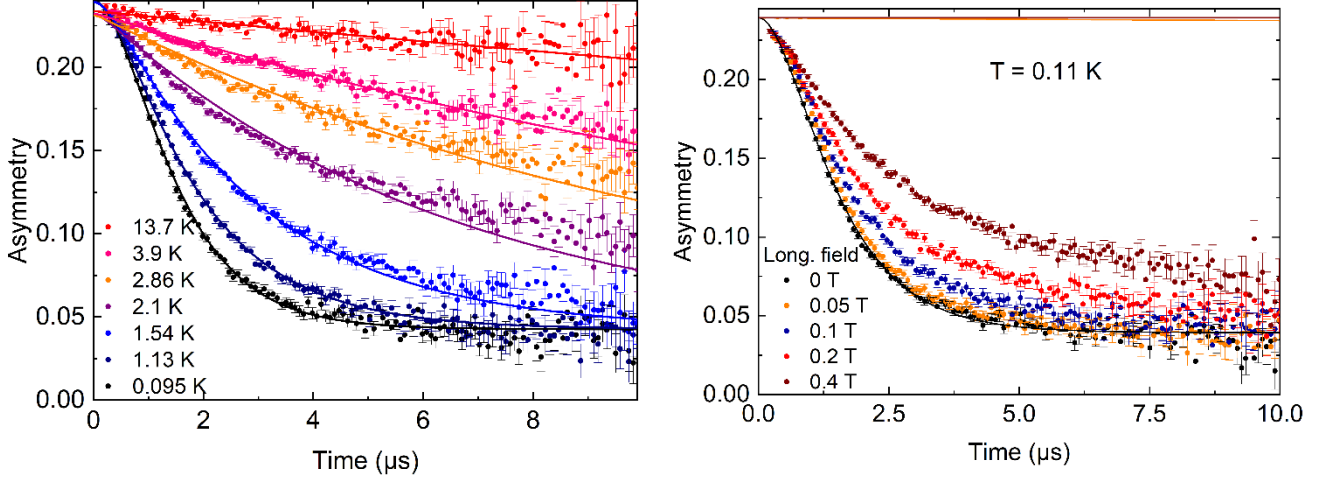


Figure 14. Left: Muon decay asymmetry in a small 0.002 T field applied parallel to muon beam polarization to decouple small nuclear fields in $6\text{H-Sr Ba}_{2.5}\text{Sr}_{0.5}\text{NiSb}_2\text{O}_9$ at various temperatures. Lines are fits described in the text. Right: Muon decay asymmetry with an applied longitudinal magnetic field. The nearly flat orange and brown lines show the expected relaxation at 0.05 T and 0.4 T from the model used to fit the zero field data (black line).

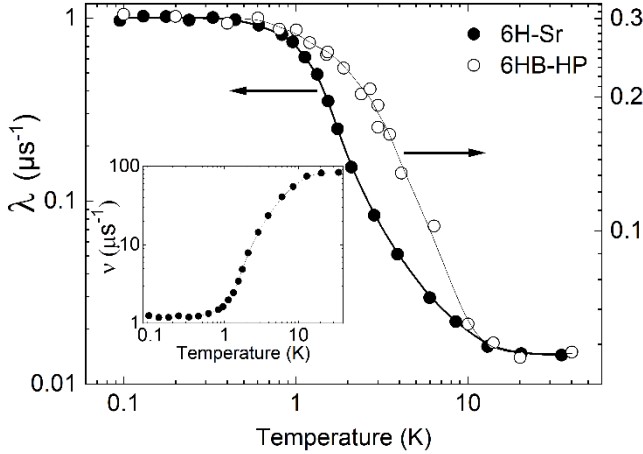


Figure 15. Inset: temperature dependence of the fluctuation rate v obtained from the fits of the zero field relaxation shown in figure 14 (left panel). Main panel: comparison of the temperature dependence of the relaxation rates $\lambda \propto 1/v$ in the 6HB-HP $\text{Ba}_3\text{SrNiSb}_2\text{O}_9$ (from [24]) and 6H-Sr $\text{Ba}_{2.5}\text{Sr}_{0.5}\text{NiSb}_2\text{O}_9$ (this study) phases.

IV. DISCUSSION

We first explain why both Ba/Sr substitution and physical pressures lead to the same 6H with Sb_2O_9 pairs \rightarrow 6H with NiSbO_9 pairs \rightarrow 3C sequence of structural phases in $\text{Ba}_3\text{NiSb}_2\text{O}_9$. The substitution of Sr^{2+} for Ba^{2+} in $\text{Ba}_3\text{NiSb}_2\text{O}_9$ causes the Goldschmidt tolerance factor to decrease. In a perovskite-like ABO_3 oxide, the tolerance factor can be written as $t = \frac{(r_A + r_O)}{\sqrt{2}(r_B + r_O)}$ where r_A and r_B are the average radii of the A and B sites, respectively, and r_O is the radius of oxide ion [45]. Hexagonal 6H structures, which can accommodate large A cations and short B-B distances in pairs of face-sharing octahedra, are observed when $t > 1$. For t equal or close to 1, 3C structures with cubic symmetry occur. Distortions to lower symmetries are expected when the A-site cation becomes too small for the cubo-octahedral cavities, i.e. when t decreases further [46]. For $\text{Ba}_{3-x}\text{Sr}_x\text{NiSb}_2\text{O}_9$, also written as $[\text{Ba}_{(3-x)/3}\text{Sr}_{x/3}][\text{Ni}_{1/3}\text{Sb}_{2/3}]\text{O}_3$, the tolerance factor calculated using Shannon's ionic radii [25] decreases from $t = 1.048$ in AP 6HA $\text{Ba}_3\text{NiSb}_2\text{O}_9$ ($x = 0$) to $t = 0.989$ in the double perovskite $\text{Sr}_3\text{NiSb}_2\text{O}_9$ ($x = 3$) and is equal to 1.039 and 1.024 for 6H-Sr $\text{Ba}_{2.5}\text{Sr}_{0.5}\text{NiSb}_2\text{O}_9$ and 3C-Sr $\text{Ba}_{1.75}\text{Sr}_{1.25}\text{NiSb}_2\text{O}_9$, respectively. In the 3C-type region, the crystal structure evolves from cubic (S.G. $Fm\bar{3}m$) for $x = 1.25$ to monoclinic (S.G. $P2_1/n$) for $x = 3$. Other perovskite-related oxides experience similar structural changes as the tolerance factor decreases. For instance, partial substitution of Sr for Ba in $\text{Ba}_3\text{ZnTiWO}_9$ ($t = 1.039$) destabilizes the 6H crystal structure, and the Sr substituted compound with $t = 1.027$ forms in the 3C cubic structure [47]. Also, a sequence of phases $Fm\bar{3}m \rightarrow I4/m \rightarrow I2/m \rightarrow P2_1/n$, which are associated with the introduction of cooperative tilting of the corner-sharing octahedra, has been reported for double perovskite systems with increasing Ba/Sr substitution rates [26,28]. Similar trends are observed as the physical pressure increases because pressure tends to decrease the tolerance factor if the A-site cations are more compressible than the B-site ions in the ABO_3 oxide [48]. This explains why both chemical and physical pressures lead to the same sequence of structural phases in $\text{Ba}_3\text{NiSb}_2\text{O}_9$ which contains large and compressible Ba^{2+} on the A-site.

Although the average structures of 6H-Sr $\text{Ba}_{2.5}\text{Sr}_{0.5}\text{NiSb}_2\text{O}_9$ and 6HB-HP $\text{Ba}_3\text{NiSb}_2\text{O}_9$ are described using the same $P6_3/mmc$ model, electron diffraction results (this work and ref. [23]) suggest that their actual crystal symmetries are different. This difference, which cannot be explained on the basis of the t factor alone, is probably associated with different Ni-Sb dumbbells arrangements, and indicates that the substitution-induced chemical pressure is not equivalent to the HP-HT treatment with relaxed physical pressure. In this respect, we note that

the 6H-Sr phase prepared at AP conditions is expected to be thermodynamically stable while perovskite oxides produced at HP can be metastable at AP and room temperature [48].

We now turn to the magnetic properties of the 6H-Sr phase $\text{Ba}_{2.5}\text{Sr}_{0.5}\text{NiSb}_2\text{O}_9$. Thermodynamic and μSR results obtained earlier for pure 6HB-HP [12,24] and presented here for the AP 6H-Sr phase display qualitatively similar behaviors, albeit with some small differences. The absolute value of the Weiss temperature is slightly smaller; the effective moment is comparable to those previously found for the HP 6HB phase. Although still poorly understood, the μSR relaxation plateau attributed to persistent dynamics has been taken for long as a hallmark of spin-liquid behavior. We notice that the latter occurs at lower temperature for the AP 6H-Sr sample. It is reasonable to think that these small differences result from some Sr-induced additional disorder and a slightly modified and perhaps more complex scheme of interactions, as commented on below. We note that a previous neutron study [29] did not find - within the accuracy of the 6HB-HP data - any difference between the two 6H phases and gave evidence for shallow maxima in the structure factor $S(\mathbf{q})$ at arbitrary positions in the Brillouin zone for a triangular lattice. The results approached the predictions for a $U(1)$ gapless QSL state for $S = 1$ on the triangular lattice but failed to reproduce the position of the maxima at the K-points of the Brillouin zone. From the study by Cheng et al. [12], the observed T-linear specific heat as $T \rightarrow 0$ is also an important result which altogether with the NMR study of the 6HB-HP phase, also led to the conclusion of a gapless spin liquid ground state [24]. Several interpretations of the NMR data were discussed within (i) the triangular model incorporating bi-quadratic, next nearest neighbor and interlayer exchanges as well as single ion anisotropy which did not reproduce the gapless $1/T_1$ and the lineshapes from the experiments or (ii) a J_1 - J_2 honeycomb buckled model which will be discussed below in light of theoretical progress accomplished since then. The microscopic origin of this QSL state was therefore not fully understood and magnetic dilution or bond randomness were not considered in the corresponding paper [24].

In the 6H-Sr phase, the structural disorder suggested by our diffraction data and HAAF-STEM images is essentially associated with the Ni-Sb dumbbell arrangement in a well-crystallized 6H-type triple-perovskite material. As explained in section III.A, our results are consistent with either a random orientation of the dumbbells over a crystallite or nanosized chemical correlations for the dumbbell arrangement within the a,b planes. In the latter case, one could deal with a nano-sized triangular lattice of Ni^{2+} . In the former case, a random up or down vertical orientation of the dumbbells within a $(\text{NiSbO}_9)_\infty$ bilayer would imply that 50% of

flipped Ni-Sb dumbbells dilute the triangular lattice of magnetic $S = 1$ cations originally reported in ref. [12] (shown in Fig. 1(a)) and that the flipped dumbbells insert Ni^{2+} into the adjacent parallel triangular layer of Sb within the same $(\text{NiSbO}_9)_\infty$ bilayer. The possible nearest-neighbor super-exchange pathways in 6HB-HP and 6H-Sr phases are depicted in Fig. 16. More details on the super-exchange angles and distances can be found in the Supplemental Material [30]. Because the main super-super exchange couplings in the c -direction occur across the nonmagnetic layers of SbO_6 octahedra, the structure would contain a diluted J_1 - J_2 buckled honeycomb lattice consisting of two half-depleted triangular lattices sandwiching a layer of SbO_6 octahedra. The intralayer exchange J_2 in a triangular layer can be viewed as the next-nearest neighbor interaction on the buckled honeycomb, and the interlayer exchange J_1 corresponds to the nearest neighbour interaction for the buckled honeycomb. It is likely that the situation might be intermediate, interpolating between a diluted triangular lattice and a diluted J_1 - J_2 honeycomb model. On a general footing, this points towards the need to consider the introduction of disorder in the physical interpretation of the observed properties.

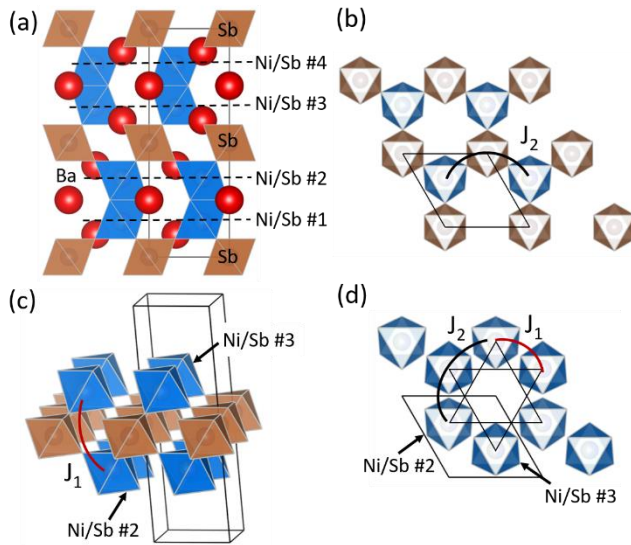


Figure 16. Nearest-neighbor Ni^{2+} - Ni^{2+} interactions in the $P6_3/mmc$ crystal structures of 6HB-HP $\text{Ba}_3\text{NiSb}_2\text{O}_9$ [23] or 6H-Sr $\text{Ba}_{2.5}\text{Sr}_{0.5}\text{NiSb}_2\text{O}_9$ (this work) assuming disorder for the Ni-Sb dumbbell arrangement. SbO_6 and NiSbO_9 bi-octahedra (Ni-Sb dumbbells) are colored brown and blue, respectively. **(a)** View along the b axis. **(b)** In-plane J_2 interaction in one of the triangular plane of $(\text{Ni/Sb})\text{O}_6$ octahedra which are connected by their vertices to single SbO_6 octahedra. **(c)** Inter-plane J_1 interaction across a layer of nonmagnetic SbO_6 octahedra. **(d)** The J_1 - J_2 buckled honeycomb lattice formed by two adjacent triangular planes of $(\text{Ni/Sb})\text{O}_6$

octahedra. Here nonmagnetic SbO_6 octahedra are omitted for clarity. Distances and angles for J_1 and J_2 superexchange pathways are given in Supplemental Material [30].

We first come back to the initial proposal by Cheng et al. [12] of an undiluted triangular lattice, which was also considered in ref. [29]. Studies of the triangular lattice have been much revived after the discovery of a spin liquid-like state at low temperatures in the rare-earth compound YbMgGaO_4 [1–3]. We note that in the absence of disorder, stabilizing a spin-liquid state requires a large exchange anisotropy [49]. In contrast with that case, working with a $3d$ transition-metal ion such as Ni^{2+} in a weak octahedral crystal field makes such a scenario unrealistic as supported by our ESR data obtained for 6HB-HP $\text{Ba}_3\text{NiSb}_2\text{O}_9$. These ESR data and their analyses are presented in the Supplemental Material [30].

With its even lower coordination, $z = 3$ versus 6 in the triangular case, the honeycomb lattice is more prone to a spin liquid ground state under isotropic antiferromagnetic interactions provided that frustration is introduced. This is realized in the J_1 - J_2 honeycomb model which has been extensively studied for $S = 1/2$ by many theoretical techniques. Although not firmly established, a consensus has emerged that in a narrow range above $J_2/J_1 \approx 0.23$, a gapless QSL phase could be more favorable than a well-established gapped plaquette valence bond order found to occur for ratios of J_2/J_1 up to ≈ 0.36 [50–53] [54]. While less is known for the $S = 1$ case, it seems that in the competition between the QSL and the gapped plaquette phase, the latter might be favored which is contrary to our experimental results [50,53]. Of course, in order to proceed with a detailed comparison with these numerical results, one should get first some estimate of this ratio through ab-initio calculations of the exchange parameters which are beyond the scope of this paper. Yet, we note that the small difference in the exchange paths for J_1 and J_2 described in the Supplemental Material [30], does not support the idea of a fine tuning of the J_2/J_1 ratio required for that alleged QSL phase.

Disorder could also be an important player in the interpretation of the absence of magnetic order as was also heavily debated in the context of the YbMgGaO_4 triangular compound [4,5,55]. The scenario of a J_1 - J_2 disordered honeycomb lattice in 6HB-HP was first discussed at length in ref. [56] with a proposal for a gapless random singlet phase with orphan spins under the combined effect of frustration and disorder. This proposal seems consistent with published results for 6HB-HP: an upper bound of the disorder parameter $\Delta = \Delta J/J = 0.25$ was estimated from the ^{121}Sb NMR linewidth [24] and could be just enough to stabilize such a phase as

predicted by Uematsu and Kawamura [56] in a revised version from ref. [57,58] earlier considered in ref. [24]. Several experimental findings conspire in favor of such a scenario, a linear specific heat was reported [12], peaks of the INS structure factor [29] are smeared out and found at locations different from usual peaks at Γ or K points in the Brillouin zone for the ordered or plaquette phases.

In a more general context where frustration promotes the formation of local singlets, e.g. for a valence bond solid phase, Kimchi et al. [6] have shown how even weak disorder can nucleate $S=1/2$ topological defects and lead to a random spin network with gapless low energy excitations. Starting for example from a honeycomb lattice and the case where the ratio J_2/J_1 does not lead to a QSL or a valence bond scenario in the absence of disorder, we may speculate that disorder could then be the driving force towards a QSL state. This scenario has been involved in the well-studied case of YbMgGaO_4 where a power law behavior of the specific heat is found and the calculated structure factor displays a shallow maximum when second neighbor interactions are included [6]. The similarity with our data shows that structural disorder model might be then the right track to explain the spin-liquid like behavior in the 6HB-HP and 6H-Sr phases.

The cubic crystal structure of 3C-Sr $\text{Ba}_{1.75}\text{Sr}_{1.25}\text{NiSb}_2\text{O}_9$ is very similar to that of 3C-HP $\text{Ba}_3\text{NiSb}_2\text{O}_9$ obtained at 9 GPa [12] so that these compounds should share common features. The Curie-Weiss temperatures θ are indeed comparable and the higher absolute value of θ in 3C-Sr phase correlates with its smaller cell volume. For both compounds, magnetic specific heats indicated significant magnetic entropy and quadratic behaviors $C_M = \gamma T^2$ at low temperatures whereas no sign of magnetic transition down to the base temperatures (0.35 K or 2 K) was found in the specific heat data. However, our μSR and ^{131}Sb NMR investigation clearly revealed the occurrence of a transition to a magnetic ordered structure below $T_m \approx 11$ K in 3C-Sr with a substantial disorder. In the context of what should be a 3D interaction scheme for a face-centered cubic (FCC) lattice, the T^2 behavior of the specific heat instead of a T^3 behavior expected for standard 3D spin waves remains to be explained. In 3C-Sr and 3C-HP, the $(\text{Ba,Sr})_2\text{BB}'\text{O}_6$ double perovskite structure is made of two B and B' interpenetrating FCC lattices where B and B' sites are occupied by Sb and $(\text{Ni}_{2/3}\text{Sb}_{1/3})$ atoms, respectively. Therefore, both 3C-Sr and 3C-HP compounds contain a site-diluted FCC sublattice of spin-1 Ni^{2+} cations with 67% site occupancy, which is much higher than the site percolation threshold for a FCC ($p_c^{\text{site}} \approx 20\%$). Thus, either a J_1 or a J_1 - J_2 model on the 1/3-depleted FCC lattice, where J_1 and J_2 are the nearest neighbor (NN) and next-nearest neighbor (NNN) interactions (displayed in

Fig. 2), respectively, are likely to be relevant for explaining the magnetic behaviors. The possible NN and NNN super-super-exchange pathways for J_1 and J_2 are described in the Supplemental Material [30]. J_1 interactions occur along Ni-O-O-Ni and 90° Ni-O-Sb-O-Ni pathways with a Ni-Ni distance of 5.71 or 5.77 Å. The former path, which is the shortest, is commonly found to be AF and dominant over the second one [59,60]. J_2 corresponds to a linear Ni-O-Sb-O-Ni pathway with a Ni-Ni distance of 8.08 - 8.15 Å. The magnetic behaviors of perovskite oxides that contain octahedral Ni^{2+} and diamagnetic Sb^{5+} , such as $\text{Sr}_3\text{NiSb}_2\text{O}_9$, SrLaNiSbO_6 , and $\text{La}_3\text{Ni}_2\text{SbO}_9$, indicate that J_1 and J_2 are AF and that J_2 is weak due to the completely filled Sb^{5+} 4d orbitals [37,61]. For a Heisenberg J_1 - J_2 model on a FCC lattice with J_2/J_1 close to zero, theoretical and experimental work for classical spins clearly point to the stabilization of AF ordering with a stacking of AF planes which depends on the J_2/J_1 ratio and which can be classified as type-I, type-II or type-III [62–64]. Little change is found when one goes from the classical to the quantum case, see e.g. [64]. We note that the case $J_2 \approx 0$ leads to a remarkable depression of T_N with respect to larger values of J_2/J_1 [64]. All of this is clearly consistent with our findings of ordering at low temperatures and a sizeable frustration ratio. Moreover, the dilution of the FCC magnetic lattice is clearly in line with the signatures of a substantial disorder of the magnetic structure revealed by the distribution of μSR relaxation rates, the NMR line broadening above T_m and the absence of long-lived oscillation of the μ^+ asymmetry and correspondingly the NMR lineshape below T_m . Finally, a broad maximum of the relaxation rate occurring only around $0.8 T_m$ is also seen in the case of triangular chromates [38,39] where a similar observation is clearly established and argued to be a signature of frustration through the persistence of fluctuations well below T_m . Our experimental results are similar to 5d B-site ordered double perovskites containing only one magnetic $S = 1$ cation, namely $\text{La}_2\text{LiReO}_6$ and Ba_2YReO_6 [65], although the spin-orbit coupling might play a major role there in the selection of the ground state. While weak local lattice distortions and possible associated spin Hamiltonian randomness induced by Ba/Sr substitution in 3C-Sr might support the idea of a physical difference between the two 3C compounds, as reflected in the susceptibility and specific heat data, it is very surprising not to find any hint of a transition in 3C-HP $\text{Ba}_3\text{NiSb}_2\text{O}_9$ in the context of the present discussion. A larger low-T Curie term from orphan spins could provide a naïve explanation for the lack of signature in the FC-ZFC susceptibility data of ref. [12]. This certainly calls for a more systematic study of the susceptibility at lower fields and a deeper investigation through μSR , NMR or low-temperature neutron diffraction.

V. CONCLUDING REMARKS

As in other perovskite oxides, the commonly observed 6H-3C transformation under physical pressure occurs when the crystal structure of $\text{Ba}_3\text{NiSb}_2\text{O}_9$ is gradually compressed by Sr/Ba chemical substitution. Generally speaking, chemical pressure can provide a simple tool for elaborating perovskite materials with unexplored or modulated electronic properties.

By combining several diffraction techniques, high-resolution Z-contrast imaging and atomic resolution elemental mapping, we have shown that the crystal structures of the 6HB-HP $\text{Ba}_3\text{NiSb}_2\text{O}_9$ and 6H-Sr phase feature undistorted triangular lattices of NiSbO_9 dumbbells. However, the lack of long-range order in the orientation of the dumbbells and the fact that it is not possible to identify short-range chemical correlations make it difficult to analyze the spin-liquid like magnetic behavior. The dumbbell disorders certainly lead to complex frustrated magnetic networks and therefore to deviations from clean antiferromagnetic models such as the triangular or the frustrated J_1 - J_2 honeycomb. We discussed how this disorder might be the seed for the spin liquid-like behavior which seems to be relevant in a broader context. The situation regarding the 3C phases appears simpler because they can be considered as realizations of a diluted FCC lattice of real $S = 1$ spins. Further, our results for the 3C-Sr indicate clear differences relative to the pure HP 3C system and therefore call for further investigations of these 3C phases.

VI. ACKNOWLEDGMENTS

We would like to thank P. Bordet, B. Fåk, Arnaud Ralko, Sylvain Capponi, and B. Gaulin for useful discussions. This work was supported in part by the French Agence Nationale de la Recherche under Grants Nos. ANR-12-BS04-0021 ‘SPINLIQ’ and ANR-18-CE30-0022-04 ‘LINK’. Funded by the French Contrat Plan État-Région and the European Regional Development Fund of Pays de la Loire, the CIMEN Electron Microscopy Center in Nantes is greatly acknowledged. This research also involved the geochemical analysis facility at Laboratoire de Planétologie et Géosciences (UMR 6112). A.Z. acknowledges the financial support of the Slovenian Research Agency under program No. P1-0125 and projects No. BI-US/22-24-065, No. J1-2461, and No. N1-0148. The National High Magnetic Field Laboratory

is supported by National Science Foundation through NSF/DMR-1644779 and the State of Florida.

REFERENCES & FOOTNOTES

- [1] Y. Li, H. Liao, Z. Zhang, S. Li, F. Jin, L. Ling, L. Zhang, Y. Zou, L. Pi, Z. Yang, J. Wang, Z. Wu, and Q. Zhang, *Gapless Quantum Spin Liquid Ground State in the Two-Dimensional Spin-1/2 Triangular Antiferromagnet YbMgGaO₄*, Sci. Rep. **5**, 1 (2015).
- [2] Y. Li, G. Chen, W. Tong, L. Pi, J. Liu, Z. Yang, X. Wang, and Q. Zhang, *Rare-Earth Triangular Lattice Spin Liquid: A Single-Crystal Study of YbMgGaO₄*, Phys. Rev. Lett. **115**, 167203 (2015).
- [3] Y. Li, D. Adroja, P. K. Biswas, P. J. Baker, Q. Zhang, J. Liu, A. A. Tsirlin, P. Gegenwart, and Q. Zhang, *Muon Spin Relaxation Evidence for the U(1) Quantum Spin-Liquid Ground State in the Triangular Antiferromagnet YbMgGaO₄*, Phys. Rev. Lett. **117**, 097201 (2016).
- [4] Z. Zhu, P. A. Maksimov, S. R. White, and A. L. Chernyshev, *Disorder-Induced Mimicry of a Spin Liquid in YbMgGaO₄*, Phys. Rev. Lett. **119**, 157201 (2017).
- [5] Y. Li, P. Gegenwart, and A. A. Tsirlin, *Spin Liquids in Geometrically Perfect Triangular Antiferromagnets*, J. Phys. Condens. Matter **32**, 224004 (2020).
- [6] I. Kimchi, A. Nahum, and T. Senthil, *Valence Bonds in Random Quantum Magnets: Theory and Application to YbMgGaO₄*, Phys. Rev. X **8**, 031028 (2018).
- [7] Y. Shirata, H. Tanaka, A. Matsuo, and K. Kindo, *Experimental Realization of a Spin-1/2 Triangular-Lattice Heisenberg Antiferromagnet*, Phys. Rev. Lett. **108**, 057205 (2012).
- [8] H. D. Zhou, Cenke Xu, A. M. Hallas, H. J. Silverstein, C. R. Wiebe, I. Umegaki, J. Q. Yan, T. P. Murphy, J.-H. Park, Y. Qiu, J. R. D. Copley, J. S. Gardner, and Y. Takano, *Successive Phase Transitions and Extended Spin-Excitation Continuum in the S=1/2 Triangular-Lattice Antiferromagnet Ba₃CoSb₂O₉*, Phys. Rev. Lett. **109**, 267206 (2012).
- [9] H. D. Zhou, E. S. Choi, G. Li, L. Balicas, C. R. Wiebe, Y. Qiu, J. R. D. Copley, and J. S. Gardner, *Spin Liquid State in the S=1/2 Triangular Lattice Ba₃CuSb₂O₉*, Phys. Rev. Lett. **106**, 147204 (2011).
- [10] S. Nakatsuji, K. Kuga, K. Kimura, R. Satake, N. Katayama, E. Nishibori, H. Sawa, R. Ishii, M. Hagiwara, F. Bridges, T. U. Ito, W. Higemoto, Y. Karaki, M. Halim, A. A. Nugroho, J. A. Rodriguez-Rivera, M. A. Green, and C. Broholm, *Spin-Orbital Short-Range Order on a Honeycomb-Based Lattice*, Science **336**, 559 (2012).
- [11] J. A. Quilliam, F. Bert, E. Kermarrec, C. Payen, C. Guillot-Deudon, P. Bonville, C. Baines, H. Luetkens, and P. Mendels, *Singlet Ground State of the Quantum Antiferromagnet Ba₃CuSb₂O₉*, Phys. Rev. Lett. **109**, (2012).
- [12] J. G. Cheng, G. Li, L. Balicas, J. S. Zhou, J. B. Goodenough, C. Xu, and H. D. Zhou, *High-Pressure Sequence of Ba₃NiSb₂O₉ Structural Phases: New S=1 Quantum Spin Liquids Based on Ni²⁺*, Phys. Rev. Lett. **107**, 197204 (2011).
- [13] T. Susuki, N. Kurita, T. Tanaka, H. Nojiri, A. Matsuo, K. Kindo, and H. Tanaka, *Magnetization Process and Collective Excitations in the S=1/2 Triangular-Lattice Heisenberg Antiferromagnet Ba₃CoSb₂O₉*, Phys. Rev. Lett. **110**, 267201 (2013).
- [14] J. Ma, Y. Kamiya, T. Hong, H. B. Cao, G. Ehlers, W. Tian, C. D. Batista, Z. L. Dun, H. D. Zhou, and M. Matsuda, *Static and Dynamical Properties of the Spin-1/2 Equilateral Triangular-Lattice Antiferromagnet Ba₃CoSb₂O₉*, Phys. Rev. Lett. **116**, 087201 (2016).

- [15] S. Ito, N. Kurita, H. Tanaka, S. Ohira-Kawamura, K. Nakajima, S. Itoh, K. Kuwahara, and K. Kakurai, *Structure of the Magnetic Excitations in the Spin-1/2 Triangular-Lattice Heisenberg Antiferromagnet $Ba_3CoSb_2O_9$* , Nat. Commun. **8**, 1 (2017).
- [16] Y. Han, M. Hagiwara, T. Nakano, Y. Nozue, K. Kimura, M. Halim, and S. Nakatsuji, *Observation of the Orbital Quantum Dynamics in the Spin-1/2 Hexagonal Antiferromagnet $Ba_3CuSb_2O_9$* , Phys. Rev. B **92**, 180410 (2015).
- [17] A. Smerald and F. Mila, *Disorder-Driven Spin-Orbital Liquid Behavior in the $Ba_3XSb_2O_9$ Materials*, Phys. Rev. Lett. **115**, 147202 (2015).
- [18] Yusuke Wakabayashi, Daisuke Nakajima, Yuki Ishiguro, Kenta Kimura, Tsuyoshi Kimura, Satoshi Tsutsui, Alfred Q. R. Baron, Kouichi Hayashi, Naohisa Happo, Shinya Hosokawa, Kenji Ohwada, and Satoru Nakatsuji, *Chemical and Orbital Fluctuations in $Ba_3CuSb_2O_9$* , Phys. Rev. B **93**, 245117 (2016).
- [19] M. Altmeyer, F. Mila, A. Smerald, and R. Valentí, *Cu-Sb Dumbbell Arrangement in the Spin-Orbital Liquid Candidate $Ba_3CuSb_2O_9$* , Phys. Rev. B **96**, 115116 (2017).
- [20] H. Man, M. Halim, H. Sawa, M. Hagiwara, Y. Wakabayashi, and S. Nakatsuji, *Spin-Orbital Entangled Liquid State in the Copper Oxide $Ba_3CuSb_2O_9$* , J. Phys. Condens. Matter **30**, 443002 (2018).
- [21] P. D. Battle, C. W. Jones, P. Lightfoot, and R. Strange, *High-Pressure Phase Transitions in the 6H Perovskites $Ba_3MSb_2O_9$ ($M = Mg, Ni, Zn$)*, J. Solid State Chem. **85**, 144 (1990).
- [22] A. J. Jacobson and A. J. Calvert, *A Powder Neutron Diffraction Study of Cation Ordering in 6H $Ba_3Sb_2NiO_9$* , J. Inorg. Nucl. Chem. **40**, 447 (1978).
- [23] C. Darie, C. Lepoittevin, H. Klein, S. Kodjikian, P. Bordet, C. V. Colin, O. I. Lebedev, C. Deudon, and C. Payen, *A New High Pressure Form of $Ba_3NiSb_2O_9$* , J. Solid State Chem. **237**, 166 (2016).
- [24] J. A. Quilliam, F. Bert, A. Manseau, C. Darie, C. Guillot-Deudon, C. Payen, C. Baines, A. Amato, and P. Mendels, *Gapless Quantum Spin Liquid Ground State in the Spin-1 Antiferromagnet 6HB $Ba_3NiSb_2O_9$* , Phys. Rev. B **93**, 214432 (2016).
- [25] R. D. Shannon, *Revised Effective Ionic Radii and Systematic Studies of Interatomic Distances in Halides and Chalcogenides*, Acta Crystallogr. A **32**, 5 (1976).
- [26] Q. Zhou, T.-Y. Tan, B. J. Kennedy, and J. R. Hester, *Crystal Structures and Phase Transitions in Sr Doped Ba_2InTaO_6 Perovskites*, J. Solid State Chem. **206**, 122 (2013).
- [27] J. Li, P. Jiang, W. Gao, R. Cong, and T. Yang, *Chemical Substitution-Induced and Competitive Formation of 6H and 3C Perovskite Structures in $Ba_{3-x}Sr_xZnSb_2O_9$: The Coexistence of Two Perovskites in $0.3 \leq x \leq 1.0$* , Inorg. Chem. **56**, 14335 (2017).
- [28] P. Kayser, S. Injac, B. J. Kennedy, T. Vogt, M. Avdeev, H. E. Maynard-Casely, and Z. Zhang, *Structural and Magnetic Properties of the Osmium Double Perovskites $Ba_{2-x}Sr_xYO_6$* , Inorg. Chem. **56**, 6565 (2017).
- [29] B. Fåk, S. Bieri, E. Canévet, L. Messio, C. Payen, M. Viaud, C. Guillot-Deudon, C. Darie, J. Ollivier, and P. Mendels, *Evidence for a Spinon Fermi Surface in the Triangular $S=1$ Quantum Spin Liquid $Ba_3NiSb_2O_9$* , Phys. Rev. B **95**, 060402 (2017).
- [30] See Supplemental Material at for details on the synthesis and characterization; super-exchange interactions; ESR study of HP 6HB $Ba_3NiSb_2O_9$, which includes Refs. [12, 23, 31, 66-79].
- [31] V. Petricek, M. Dusek, and L. Palatinus, *Crystallographic Computing System JANA2006: General Features*, Z. Für Krist. **229**, 345 (2014).
- [32] K. Momma and F. Izumi, *VESTA 3 for Three-Dimensional Visualization of Crystal, Volumetric and Morphology Data*, J. Appl. Crystallogr. **44**, 1272 (2011).
- [33] L. Palatinus, *PETS-Program for Analysis of Electron Diffraction Data; Institute of Physics of the CAS: Praha Czechia.*, (2011).

- [34] M. T. Anderson, K. B. Greenwood, G. A. Taylor, and K. R. Poeppelmeier, *B-Cation Arrangements in Double Perovskites*, Prog. Solid State Chem. **22**, 197 (1993).
- [35] G. King and P. M. Woodward, *Cation Ordering in Perovskites*, J. Mater. Chem. **20**, 5785 (2010).
- [36] M. James, J. P. Attfield, and J. Rodriguez-Carvajal, *Synthesis, Crystal Structure and Magnetism of $\text{Sr}_3\text{Sb}_2\text{NiO}_9$ - A Ferrimagnetic Perovskite*, J. Phys. Chem. Solids **56**, 1331 (1995).
- [37] P. D. Battle, C.-M. Chin, S. I. Evers, and M. Westwood, *Structure and Magnetism of $\text{Sr}_3\text{NiSb}_2\text{O}_9$* , J. Solid State Chem. **227**, 1 (2015).
- [38] A. Olariu, P. Mendels, F. Bert, B. G. Ueland, P. Schiffer, R. F. Berger, and R. J. Cava, *Unconventional Dynamics in Triangular Heisenberg Antiferromagnet NaCrO_2* , Phys. Rev. Lett. **97**, 167203 (2006).
- [39] K. Somesh, Y. Furukawa, G. Simutis, F. Bert, M. Prinz-Zwick, N. Büttgen, A. Zorko, A. A. Tsirlin, P. Mendels, and R. Nath, *Universal Fluctuating Regime in Triangular Chromate Antiferromagnets*, Phys. Rev. B **104**, 104422 (2021).
- [40] R. S. Hayano, Y. J. Uemura, J. Imazato, N. Nishida, T. Yamazaki, and R. Kubo, *Zero- and Low-Field Spin Relaxation Studied by Positive Muons*, Phys. Rev. B **20**, 850 (1979).
- [41] A. Keren, *Generalization of the Abragam Relaxation Function to a Longitudinal Field*, Phys. Rev. B **50**, 10039 (1994).
- [42] Y. J. Uemura, A. Keren, K. Kojima, L. P. Le, G. M. Luke, W. D. Wu, Y. Ajiro, T. Asano, Y. Kuriyama, M. Mekata, H. Kikuchi, and K. Kakurai, *Spin Fluctuations in Frustrated Kagomé Lattice System $\text{SrCr}_8\text{Ga}_4\text{O}_{19}$ Studied by Muon Spin Relaxation*, Phys. Rev. Lett. **73**, 3306 (1994).
- [43] D. Bono, P. Mendels, G. Collin, N. Blanchard, F. Bert, A. Amato, C. Baines, and A. D. Hillier, *μSR Study of the Quantum Dynamics in the Frustrated $S=3/2$ Kagomé Bilayers*, Phys. Rev. Lett. **93**, 187201 (2004).
- [44] P. Khuntia, F. Bert, P. Mendels, B. Koteswararao, A. V. Mahajan, M. Baenitz, F. C. Chou, C. Baines, A. Amato, and Y. Furukawa, *Spin Liquid State in the 3D Frustrated Antiferromagnet $\text{PbCuTe}_2\text{O}_6$: NMR and Muon Spin Relaxation Studies*, Phys. Rev. Lett. **116**, 107203 (2016).
- [45] V. M. Goldschmidt, *Die Gesetze der Krystallochemie*, Naturwissenschaften **14**, 477 (1926).
- [46] P. M. Woodward, *Octahedral Tilting in Perovskites. II. Structure Stabilizing Forces*, Acta Crystallogr. B **53**, 1 (1997).
- [47] R. Mani, P. Selvamani, J. E. Joy, J. Gopalakrishnan, and T. K. Mandal, *Study of $\text{Ba}_3\text{M}^{\text{II}}\text{M}^{\text{IV}}\text{WO}_9$ ($\text{M}^{\text{II}} = \text{Ca, Zn}$; $\text{M}^{\text{IV}} = \text{Ti, Zr}$) Perovskite Oxides: Competition between 3C and 6H Perovskite Structures*, Inorg. Chem. **46**, 6661 (2007).
- [48] J. B. Goodenough and J. A. Kavalas, *Exploring the $\text{A}^+\text{B}^{3+}\text{O}_3$ Compounds*, J. Solid State Chem. **6**, 493 (1973).
- [49] Z. Zhu, P. A. Maksimov, S. R. White, and A. L. Chernyshev, *Topography of Spin Liquids on a Triangular Lattice*, Phys. Rev. Lett. **120**, 207203 (2018).
- [50] S.-S. Gong, W. Zhu, and D. N. Sheng, *Quantum Phase Diagram of the Spin-1 J_1 - J_2 Heisenberg Model on the Honeycomb Lattice*, Phys. Rev. B **92**, 195110 (2015).
- [51] F. Ferrari, S. Bieri, and F. Becca, *Competition between Spin Liquids and Valence-Bond Order in the Frustrated Spin-1/2 Heisenberg Model on the Honeycomb Lattice*, Phys. Rev. B **96**, 104401 (2017).
- [52] A. F. Albuquerque, D. Schwandt, B. Hetényi, S. Capponi, M. Mambrini, and A. M. Läuchli, *Phase Diagram of a Frustrated Quantum Antiferromagnet on the Honeycomb Lattice: Magnetic Order versus Valence-Bond Crystal Formation*, Phys. Rev. B **84**, 024406 (2011).

- [53] J. Merino and A. Ralko, *Role of Quantum Fluctuations on Spin Liquids and Ordered Phases in the Heisenberg Model on the Honeycomb Lattice*, Phys. Rev. B **97**, 205112 (2018).
- [54] The proposal of G. Chen et al. [G. Chen, M. Hermele, and L. Radzihovsky, Phys. Rev. Lett. **109**, 016402 (2012)] to consider being close to a quantum critical point requires a substantial single ion anisotropy and leads to a gapped state, both are not the case here.
- [55] H.-Q. Wu, S.-S. Gong, and D. N. Sheng, *Randomness-Induced Spin-Liquid-like Phase in the Spin-1/2 J_1 - J_2 Triangular Heisenberg Model*, Phys. Rev. B **99**, 085141 (2019).
- [56] K. Uematsu and H. Kawamura, *Randomness-Induced Quantum Spin Liquid Behavior in the $s = 1/2$ Random J_1 - J_2 Heisenberg Antiferromagnet on the Honeycomb Lattice*, J. Phys. Soc. Jpn. **86**, 044704 (2017).
- [57] K. Watanabe, H. Kawamura, H. Nakano, and T. Sakai, *Quantum Spin-Liquid Behavior in the Spin-1/2 Random Heisenberg Antiferromagnet on the Triangular Lattice*, J. Phys. Soc. Jpn. **83**, 034714 (2014).
- [58] T. Shimokawa, K. Watanabe, and H. Kawamura, *Static and Dynamical Spin Correlations of the $S=1/2$ Random-Bond Antiferromagnetic Heisenberg Model on the Triangular and Kagome Lattices*, Phys. Rev. B **92**, 134407 (2015).
- [59] Z. Lu, L. Ge, G. Wang, M. Russina, G. Günther, C. R. dela Cruz, R. Sinclair, H. D. Zhou, and J. Ma, *Lattice Distortion Effects on the Frustrated Spin-1 Triangular-Antiferromagnet $A_3\text{NiNb}_2\text{O}_9$ ($A=\text{Ba}$, Sr , and Ca)*, Phys. Rev. B **98**, 094412 (2018).
- [60] R. Rawl, M. Lee, E. S. Choi, G. Li, K. W. Chen, R. Baumbach, C. R. dela Cruz, J. Ma, and H. D. Zhou, *Magnetic Properties of the Triangular Lattice Magnets $A_4B'B_2\text{O}_{12}$ ($A=\text{Ba}$, Sr , La ; $B'=\text{Co}$, Ni , Mn ; $B=\text{W}$, Re)*, Phys. Rev. B **95**, 174438 (2017).
- [61] C.-M. Chin, P. D. Battle, A. L. Goodwin, and A. Wildes, *Short-Range Cation and Spin Ordering in the Relaxor Ferromagnet $\text{La}_3\text{Ni}_2\text{SbO}_9$ Studied by Polarized-Neutron Scattering and Monte-Carlo Methods*, J. Solid State Chem. **278**, 120920 (2019).
- [62] M. S. Seehra and T. M. Giebultowicz, *Magnetic Structures of Fcc Systems with Nearest-Neighbor and next-Nearest-Neighbor Exchange Interactions*, Phys. Rev. B **38**, 11898 (1988).
- [63] J. S. Smart, *Effective Field Theories of Magnetism* (Saunders, Philadelphia; London, 1966).
- [64] N.-N. Sun and H.-Y. Wang, *The J_1 - J_2 Model on the Face-Centered-Cubic Lattices*, J. Magn. Magn. Mater. **454**, 176 (2018).
- [65] Tomoko Aharen, John E. Greedan, Craig A. Bridges, Adam A. Aczel, Jose Rodriguez, Greg MacDougall, Graeme M. Luke, Vladimir K. Michaelis, Scott Kroeker, Chris R. Wiebe, Haidong Zhou, and Lachlan M. D. Cranswick, *Structure and Magnetic Properties of the $S=1$ Geometrically Frustrated Double Perovskites $\text{La}_2\text{LiReO}_6$ and Ba_2YReO_6* , Phys. Rev. B **81**, 064436 (2010).
- [66] G. E. Pake, *Paramagnetic resonance: an introductory monograph* (WA Benjamin, New York, 1962).
- [67] A. Zorko, *Determination of Magnetic Anisotropy by EPR*, in Topics From EPR Research, edited by A. M. Maghraby (IntechOpen, London, 2019).
- [68] M. S. Seehra and T. G. Castner, *The paramagnetic line width in $\text{Cu}(\text{HCOO})_2 \cdot 4\text{H}_2\text{O}$* , Phys. Kondens. Materie **7**, 185–200 (1968).
- [69] D. L. Huber and M. S. Seehra, *Contribution of the spin-phonon interaction to the paramagnetic resonance linewidth of CrBr_3* , J. Phys. Chem. Solids **36**, 723 (1975).
- [70] M. S. Seehra, M. M. Ibrahim, V. S. Babu, and G. Srinivasan, *The linear temperature dependence of the paramagnetic resonance linewidth in the manganate perovskites $\text{La}_{0.67}\text{Sr}_{0.33}\text{MnO}_3$ and $\text{La}_{0.62}\text{Bi}_{0.05}\text{Ca}_{0.33}\text{MnO}_3$* , J. Phys.: Condens. Matter **8**, 11283 (1996).

- [71] J. Deisenhofer, S. Schaile, J. Teyssier, Z. Wang, M. Hemmida, H.-A. Krug von Nidda, R. M. Eremina, M. V. Eremin, R. Viennois, E. Giannini, D. van der Marel, and A. Loidl, *Electron spin resonance and exchange paths in the orthorhombic dimer system Sr_2VO_4* , Phys. Rev. B **86**, 214417 (2012).
- [72] A. Zorko, D. Arčon, H. van Tol, L. C. Brunel, and H. Kageyama, *X-band ESR determination of Dzyaloshinsky-Moriya interaction in the two-dimensional $\text{SrCu}_2(\text{BO}_3)_2$ system*, Phys. Rev. B **69**, 174420 (2004).
- [73] A. Zorko, F. Bert, A. Ozarowski, J. van Tol, D. Boldrin, A. S. Wills, and P. Mendels, *Dzyaloshinsky-Moriya interaction in vesignieite: A route to freezing in a quantum kagome antiferromagnet*, Phys. Rev. B **88**, 144419 (2013).
- [74] A. Zorko, D. Arčon, A. Lappas, J. Giapintzakis, C. Saylor, and L. C. Brunel, *Effect of vacancy doping on the Haldane spin-liquid state in $\text{PbNi}_{2-x}\text{Mg}_x\text{V}_2\text{O}_8$* , Phys. Rev. B **65**, 144449 (2002).
- [75] M. Heinrich, H.-A. Krug Von Nidda, A. Loidl, N. Rogado, and R. J. Cava, *Potential Signature of a Kosterlitz-Thouless Transition in $\text{BaNi}_2\text{V}_2\text{O}_8$* , Phys. Rev. Lett. **91**, 137601 (2003).
- [76] Y. Maeda, K. Sakai, and M. Oshikawa, *Exact analysis of ESR shift in the spin-1/2 Heisenberg antiferromagnetic chain*, Phys. Rev. Lett. **95**, 037602 (2005).
- [77] R. Kubo and K. Tomita, *A general theory of magnetic resonance absorption*, J. Phys. Soc. Jpn. **9**, 888 (1954).
- [78] A. Zorko, S. Nellutla, J. van Tol, L. C. Brunel, F. Bert, F. Duc, J.-C. Trombe, M. A. de Vries, A. Harrison, and P. Mendels, *Dzyaloshinsky-Moriya anisotropy in the spin-1/2 kagome compound $\text{ZnCu}_3(\text{OH})_6\text{Cl}_2$* , Phys. Rev. Lett. **101**, 026405 (2008).
- [79] T. Moriya, *Anisotropic superexchange interaction and weak ferromagnetism*, Phys. Rev. **120**, 91 (1960).